Ocean Modelling 40 (2011) 14–34

Contents lists available at ScienceDirect

Ocean Modelling

journal homepage: www.elsevier.com/locate/ocemod

Investigation of IPCC AR4 coupled climate model North Atlantic mode water formation

Jessie C. Carman [a,c,*], Julie L. McClean [b,c]

[a] US Naval Academy, Annapolis, MD 21402, United States
[b] Scripps Institution of Oceanography, La Jolla, CA 92093, United States
[c] Lawrence Livermore National Laboratory, Livermore, CA 94551, United States

ARTICLE INFO

Article history:
Received 23 August 2010
Received in revised form 18 June 2011
Accepted 1 July 2011
Available online 29 July 2011

Keywords:
Coupled climate models
Ocean heat budget
Heat flux
Mode water formation
Ocean mixed layer
Subpolar Mode Water
Subtropical Mode Water
North Atlantic

ABSTRACT

The formation of mode waters in the North Atlantic was examined in the suite of ocean models that comprise the World Climate Research Programme (WCRP) Coupled Model Intercomparison Project phase 3 (CMIP3). We constructed model climatologies for 1980–1999 from the 20th century simulations, and compared their mode water properties (temperature, salinity, formation rate, volume, turnover time, heat content) with data. In these models, we found biases in both the properties of the mode waters and their formation rates. For Subpolar Mode Water (SPMW), property biases principally involved salinity errors; additionally, some models form SPMW in an anomalous region west of the British Isles, shifting the source location of waters entering the overturning cell and altering the Nordic Seas' involvement in the Meridional Overturning Circulation. For Subtropical Mode Water (STMW), property biases involved both salinity and temperature errors, while positioning of heat and water fluxes relative to the Gulf Stream and northwest Sargasso Sea influenced STMW formation rate. Deficiencies in STMW formation rate and volume produced a turnover time of 1–2 years, approximately half of that observed; these variations in mode water bulk properties imply variation in ocean heat storage and advection, and hence deficiencies in all the models' abilities to adequately respond to changes in climatic forcing.

Published by Elsevier Ltd.

1. Introduction

Climate models' predictions of future planetary conditions hinge on their ability to model physical processes in the atmosphere, ocean, land, and cryosphere. The realistic reproduction of fundamental physical processes under present climatic conditions is a necessary first step before attempting to predict future conditions as climate forcing changes. Evaluating the representation of ocean processes responsible for the storage and transportation of properties such as energy, heat, freshwater, and CO_2 in coupled models is essential when assessing their suitability for such applications. Mode waters serve as heat capacitors in the coupled atmosphere–ocean system and therefore act as an integrator of climate variability. In this study we choose to examine the formation of North Atlantic mode waters in standard configuration coupled climate models. Mode waters of the North Pacific and Southern Ocean also merit examination; however the North Atlantic was chosen as a key place to start due to its role in the meridional overturning circulation (MOC), the shallow northward flow of warm saline water and deep southward flow of colder saline water which transports a substantial amount of heat poleward in the Atlantic.

Mode waters are volumetrically important water masses that form at the ocean's surface and are characterised by nearly uniform temperature and salinity in a layer typically several hundred meters deep. Their properties are determined by ocean surface fluxes and *in situ* surface ocean properties; considerable literature documents mode water properties and changes with time (Talley, 1996; Peng et al., 2006). Generally these water masses are subsequently subducted deeper into the upper ocean and are seasonally isolated from the effects of ocean surface fluxes. Because of their large volume and nearly uniform properties, mode waters represent a near-surface reservoir of heat that is seasonally available for release back to the atmosphere and might influence the global atmospheric circulation (Kwon and Riser, 2004). With their large heat content and their ability to retain a year-to-year memory of property variations due to changing forcing conditions (Alexander and Deser, 1995; Timlin et al., 2002), mode waters represent an

* Corresponding author at: US Naval Academy, 572C Holloway Rd., Annapolis, MD 21402, United States. Tel.: +1 410 293 6668; fax: +1 410 293 3279.
E-mail address: carman@usna.edu (J.C. Carman).

1463-5003/$ - see front matter Published by Elsevier Ltd.
doi:10.1016/j.ocemod.2011.07.001

integrator of seasonal climate variations (Talley and Raymer, 1982; Talley and McCartney, 1982; Hanawa and Talley, 2001).

Subpolar Mode Waters (SPMW) are generally more than 400 m thick, but frequently range up to 600 m deep and can be as much as 1500 m deep during convection events in the Labrador Sea (McCartney and Talley, 1982). SPMWs are instrumental in the transfer of warm salty North Atlantic water from the subtropical gyre to the Nordic Seas and the Labrador Sea, with heat and freshwater fluxes modifying their properties along the way. The original description by McCartney and Talley (1982) hypothesized cyclonic advection of a homogenised water mass, the product of deep winter mixing events. This hypothesis has been partially revised by subsequent studies (e.g. Talley, 1999; Read, 2001; Brambilla and Talley, 2008). The final products of the gradual transformation are presently thought to develop from successive transformations of the water masses as they progress along various current branches of the North Atlantic Current as it travels past the Greenland–Iceland–UK Gap. The final products are the Labrador Sea Water and the dense water masses of the Nordic Seas; these waters are eventually transformed into North Atlantic Deep Water (NADW) (McCartney and Talley, 1982, 1984; Schmitz and McCartney, 1993; McCartney and Mauritzen, 2001; Brambilla et al., 2008).

North Atlantic Subtropical Mode Water (STMW), often called Eighteen Degree Water (EDW), has been studied for many years (Thompson, 1877). This water mass is associated with large surface heat and moisture loss from the ocean as a result of cold dry air outbreaks over North America. STMW is found just south of the Gulf Stream (Worthington, 1959) and is advected southward into the western subtropical gyre (Hanawa and Talley, 2001). The water mass is of uniform temperature close to 18 °C and is typically 250 m thick but can extend to 500 m in the late winter (McCartney, 1982). While STMW properties are relatively constant, the water mass shows variability on episodic, seasonal, and multi-year time scales, rendering meaningful distribution charts problematic (Talley and Raymer, 1982; Talley, 1996). A hypothesis of dynamical coupling between late winter convective formation and Gulf Stream gyre intensity has gained some observational support (Worthington, 1977). A relationship between STMW formation and the North Atlantic Oscillation (NAO) has been proposed (Joyce et al., 2000) that provides some insight into the variability of STMW properties as part of a coupled oscillator. STMW contributes water to a local vertical circulation cell within the Sargasso Sea, reheating and reconverting to surface layers in the southern Sargasso; some of the STMW also continues northward in the Gulf Stream extension (Lumpkin and Speer, 2003).

In this paper we inquire how well the ocean components of standard coupled climate models form North Atlantic SPMW and STMW. Since mode waters are heat reservoirs and integrators of climate, we wish to understand whether these models are forming mode waters of the correct density, in the correct amounts, and what the implications of any biases might be for the depiction of ocean feedbacks to the atmosphere on interannual time scales. We examine the global climate models in the World Climate Research Programme's (WCRP's) Coupled Model Intercomparison Project phase 3 (CMIP3) multi-model dataset that have been archived at the Program for Climate Model Diagnosis and Comparison (PCMDI) at Lawrence Livermore National Laboratory (LLNL) (Meehl et al., 2007).

We choose to use the framework of the surface water mass transformation calculations of Walin (1982) and Speer and Tziperman (1992) to relate atmosphere–ocean surface fluxes to water mass density changes. Doney et al. (1998) studied global surface ocean fluxes and water-mass transformation rates in coupled and uncoupled versions of the National Center for Atmospheric Research (NCAR) Coupled Climate System Model (CCSM). Using this framework Bryan et al. (2006) related changes in surface forcing with increasing CO_2 to changes in the MOC and ocean ventilation in three increasingly higher resolution configurations of CCSM version 3 (CCSM3). They looked at the time dependence of the MOC changes, and found that differences in the mean overturning strength and the response of overturning to transient forcing were well predicted by differences in the water-mass transformation rate. Marsh et al. (2005) studied water-mass transformation in the North Atlantic using an eddy-permitting Ocean Circulation and Climate Advanced Model (OCCAM) simulation, examining the role of mixing in the net formation of North Atlantic water masses and the variability of these water masses. Haines and Old (2005) studied the property and temporal variability of North Atlantic water masses in the Third Hadley Centre Coupled Ocean–Atmosphere General Circulation Model (HadCM3). Recently, Maze et al. (2009) used ocean/atmosphere model/data syntheses and surface water mass transformation maps to demonstrate the role of air–sea heat fluxes in North Atlantic STMW formation and the resulting seasonal and spatial formation/destruction cycle. Forget et al. (2011) quantified the seasonal cycle of North Atlantic STMW volume budget in the same model/data syntheses and compared calculated STMW volume with previously published estimates.

The remainder of this paper has the following organisation: Section 2 discusses the water mass transformation calculations, with Section 2.1 providing general background, and Section 2.2 explaining the water mass formation calculations applied to each model. Section 3 examines the results of these calculations: Section 3.1 compares the model water mass formation calculations (using σ_θ ranges from data) with published water mass formation rates; Section 3.2 uses σ_θ ranges appropriate to each model to determine that model's water mass formation rates and compares them with published formation rates. Section 4 discusses factors governing model mode water formation, with Section 4.1 covering SPMW, Section 4.2 covering STMW, and Section 4.3 discussing STMW heat content and turnover times. Section 5 gives conclusions. The Appendix contains a review of the development of the water mass formation methodology.

2. Methodology

2.1. Water mass transformation

Water mass characteristics in much of the global ocean are determined by initial contact with the atmosphere and subsequent transport and mixing in the ocean interior; thus the air–sea interaction processes which convert ocean surface waters from one density class to another require examination in coupled climate models. The Walin (1982) framework is used in this paper to calculate water mass transformation and formation rates. The former is the rate at which water is transformed from one density class to another via air–sea heat and freshwater fluxes. The divergence of the transformation rate yields the rate at which a given density class is created or destroyed via these fluxes (the formation rate).

A review of the development of the Walin methodology is found in the Appendix. Nurser et al. (1999), Marshall et al. (1999) and Large and Nurser (2001), among others, have expounded upon it and our explanation is based on their derivations. From Eq. (9) of the Appendix, the water mass that accumulates or is destroyed due to heat and freshwater surface fluxes between two outcropping isopycnals that differ by $d\rho$ (where ρ is potential density) is $M(\rho)$, and is known as the water mass formation rate per unit density. It can be written in terms of the water mass transformation rate (WMTR), $F(\rho)$, the integrated density input by heat and

freshwater fluxes into the surface outcrop region (Eq. (7) of the Appendix):

$$M(\rho) = -\frac{\partial F}{\partial \rho}$$

and the formation rate, or the water mass that accumulates over the year between any two isopycnals ρ and $\rho + \Delta\rho$, is

$$M(\rho)\Delta\rho = -[F(\rho + \Delta\rho) - F(\rho)].$$

From the Appendix, diapycnal density fluxes, edge fluxes, and cabbeling are considered to be small relative to $F(\rho)$. The appropriateness of these assumptions is discussed later in the paper. The relationships for water-mass formation and transformation are time-varying as explicitly described by Marshall et al. (1999), Maze et al. (2009) and Forget et al. (2011). Forget et al. (2011) presented the variation in volume budget over the seasonal cycle and Kwon and Riser (2004) observed interannual variability. In the steady state limit, the convergence of the diffusive fluxes across the bounding isopycnals balance the density gain or loss due to surface fluxes (see Appendix). This balance is expected to hold on long time scales in the global ocean where the mean state is not evolving (Marshall et al., 1999). In the unsteady case, water may change density locally due to local air–sea fluxes (Speer and Tziperman, 1992), in addition to having a diapycnal volume flux of water.

To calculate the WMTR, $F(\rho)$, we examine the density supply from the surface via the surface fluxes of heat and fresh water. The density flux in through the sea surface can be written (Speer and Tziperman, 1992)

$$f = -\frac{\alpha H}{C_p} + \rho(0,T)\beta\frac{(E-P)S}{1-S}$$

where the thermal expansion and saline contraction coefficients are

$$\alpha = -\frac{\partial\rho}{\rho\partial T}, \quad \beta = \frac{\partial\rho}{\rho\partial S}.$$

In these expressions, $\rho(S, T)$ is density, T and S are sea surface temperature and sea surface salinity, H is heat flux into the ocean, E and P are evaporation and precipitation, and C_p is the specific heat, all functions of position and time. We can obtain the total density flux (transformation rate) for some time period at one specific sea surface density class by integrating the density fluxes

$$F(\rho) = \int_{\text{time}} dt \iint_{\text{area}} f\delta(\rho - \rho_0)dA$$

This air–sea forcing is written equally well in terms of a transformation from one density class ρ to another or one buoyancy class to another. The density flux in through the sea surface can be written as a buoyancy flux $b = -g\rho/\rho_0$ out through the surface

$$b = -\frac{g\alpha H}{\rho_0 C_p} + \rho(0,T)\beta\frac{g(E-P)S}{\rho_0(1-S)}$$

which integrates over the surface to the same transformation rate with the appropriate change of sign (Speer, 1997).

2.2. Model water mass transformation calculations

North Atlantic WMTRs, $F(\rho)$, were calculated from the ocean components of the 20th century models (20C3M) in the CMIP3 archive for which monthly fields of all variables required for the WMTR calculation were available. Some details about the ocean components of these coupled simulations can be found in Table 1. Of these models, only CCCMA CGCM3.1 (both resolutions) and MIUB ECHO G, had flux adjustments over the whole domain; MRI CGCM2.3.2A had flux adjustments in the tropics only, and UKMO HADCM3/HADGEM1 compensated for freshwater imbalance due to snow accumulating over ice sheets by an appropriate water flux over ocean areas adjacent to iceberg regions. Monthly and annual transformation rates for the 20-year period 1980–1999 were obtained. This period was chosen as it was considered to be the most representative of present day conditions and is contemporaneous with climatologies based on observations from the past several decades. For each model, the 20-year annual totals were used to calculate mean and standard deviation of model mode water formation rate $M(\rho)\Delta\rho$ for both SPMW and STMW, using potential density (σ_θ) limits derived from the literature. Where multiple ensemble members of a model were archived, those results were included in the mean and standard deviation of the mode water formation rates. A σ_θ range of 27.3–27.7 kg/m^3 was used for SPMW (McCartney and Talley, 1982; Brambilla and Talley, 2008), and a σ_θ range of 26.4–26.6 kg/m^3 was used for STMW (McCartney, 1982; Talley and Raymer, 1982).

Simulated WMTR veracity was assessed by comparing model quantities with those obtained from observations by Speer et al. (1995). Their results were obtained using Levitus (1982) sea surface temperature and salinity data, and surface heat and freshwater fluxes from revised Comprehensive Ocean–Atmosphere Data Set (COADS) data (Woodruff et al., 1987; Wright, 1988; Oberhuber, 1988). The Speer et al. (1995) calculations were presented as plots of $F(\rho)$ which yielded formation rates $M(\rho)\Delta\rho$; uncertainties were obtained by recalculating with 10 W/m^2 added and subtracted at each data point. To put these uncertainties in the same mean-and-standard-deviation terms as the CMIP3 model calculations, the resulting upper and lower values (a_+ and a_-) were assumed to be limits of a rectangular distribution. The standard deviation of the distribution is then $\sigma = a/\sqrt{3}$, where $a = (a_+ - a_-)/2$ is the half-width of the interval (Taylor and Kuyatt, 1994).

3. Results

3.1. WMTR comparisons: observed σ_θ ranges

Model SPMW and STMW WMTRs, $F(\rho)$, were calculated using the σ_θ ranges that are representative of these water mass types in the real ocean. These values were subsequently compared with equivalent observed WMTRs. Fig. 1(a) shows formation rates, $M(\rho)\Delta\rho$, in Sverdrups (Sv; 1 Sverdrup = 10^6 m^3 s^{-1}) of SPMW for data and the CMIP3 models based on observed σ_θ values; Fig. 1(b) shows the same calculations for STMW. Formation rates of SPMW show large variation at these density classes; most notably, for the density classes of STMW, the models form very little mode water and the standard deviation is large, reflecting large annual variability.

The water mass transformation curves $F(\rho)$ for each model given in Fig. 2 reveal various reasons for the mismatch between mode water formation rates for each model and the data, as the grey shaded bars overlying the graphics represent observed STMW and SPMW density classes. If the models are forming water masses at these density classes, we should expect to see a negative WMTR slope as formation rate per unit density, $M(\rho) = -dF/d\rho$, in the grey-shaded region. For SPMW, all of the models form a dense water type and in most cases that water type falls within the σ_θ range of 27.3–27.7 kg/m^3, resulting in positive SPMW formation rates, $M(\rho)\Delta\rho$ (Fig. 1a). However, for notable cases (CNRM CM3, CSIRO MK 3.5, GFDL CM2.0, GFDL CM2.1, MIROC 3.2 MEDRES, MIUB ECHO G, MRI CGCM2.3.2A, and UKMO HADGEM1) the model's dense water type is more dense than SPMW in the ocean; for these models, at the density classes of observed SPMW, the model shows a positive gradient in $F(\rho)$, resulting in a small positive to strong negative calculated SPMW formation rate.

Table 1
Selected details of ocean models used in WMTR calculations.

		Flux adjustments?	SPMW σ_θ (kg/m^3)	STMW σ_θ (kg/m^3)	Eddy parameterization	Mixed-layer treatment
Canadian Centre for Climate Modeling and Analysis: T47	CCCMA CGCM3.1 (MOM 1.1)	Both heat and water flux adjustment	27.3–27.8	25.4–26.5	Gent and McWilliams (1990) with isopycnal diffusivity 1000 m^2/s, background horizontal diffusivity 100 m^2/s; vertical diffusivity 3e−5 m^2/s	
Canadian Centre for Climate Modeling and Analysis: T63	CCCMA CGCM3.1 T63	Both heat and water flux adjustment	27.3–27.8	25.5–26.6	Gent and McWilliams (1990) with isopycnal diffusivity 1000 m^2/s, background horizontal diffusivity 100 m^2/s; vertical diffusivity 3e−5 m^2/s	
Centre National de Recherches Météorologiques, France	CNRM CM3	No flux adjustment	27.7–28.5	26.2–26.9	Vertical: TKE; Horizontal: isopycnal diffusion, eddy viscosity 40,000 m^2/s for momentum and 2000 m^2/s eddy diffusivity	1.5 Turbulent closure scheme (Blanke and Delecluse, 1993)
Commonwealth Scientific and Industrial Research Organisation, Australia	CSIRO MK3.0	No flux adjustment	27.4–28.3	26.4–26.9	Vertical: modified Bryan and Lewis (1979); Adiabatic eddy-induced transport: Griffies (1998) implementation of Gent and McWilliams (1990)	Integer power vertical mixing scheme (Wilson, 2000, 2002) based on Pacanowski and Philander (1981) scheme
Commonwealth Scientific and Industrial Research Organisation, Australia	CSIRO MK3.5	No flux adjustment	27.3–28.5	26.2–27.0	Vertical: modified Bryan and Lewis (1979); Adiabatic eddy-induced transport: Griffies (1998) implementation of Gent and McWilliams (1990) and Visbeck et al., 1997 scheme to control strength of ocean eddy-induced transport coefficient κ	Integer power vertical mixing scheme (Wilson 2000, 2002) based on Pacanowski and Philander (1981) scheme; Kraus–Turner (1967) mixing due to wind-generated turbulent KE
Geophysical Fluid Dynamics Laboratory coupled model	GFDL CM2.0	No flux adjustment	27.5–28.1	26.3–27.3	Isopycnal mixing of tracers and layer thickness (Gent and McWilliams, 1990; Griffies et al., 1998; Griffies, 1998)	KPP scheme Large et al. (1994)
Geophysical Fluid Dynamics Laboratory coupled model	GFDL CM2.1	No flux adjustment	27.7–28.3	26.2–26.6	Isopycnal mixing of tracers and layer thickness (Gent and McWilliams, 1990; Griffies et al., 1998; Griffies 1998)	KPP scheme Large et al. (1994)
NASA Goddard Institute for Space Studies	GISS MODEL ER	No flux adjustment	27.5–28.2	26.3–26.6	Gent and McWilliams (1990) using Visbeck et al. (1997) coefficients as implemented by Griffies (1998)	KPP scheme Large et al. (1994)
Japan Center for Climate System Research: Model for Interdisciplinary Research on Climate	MIROC3.2 HIRES	No flux adjustment	27.2–27.9	25.7–26.7	Isopycnal layer thickness diffusion (Gent et al., 1995) and isopycnal diffusion (Cox, 1987) with weak background horizontal Laplacian diffusion	Turbulence closure scheme of Noh and Kim (1999)
Japan Center for Climate System Research: Model for Interdisciplinary Research on Climate	MIROC3.2 MEDRES	No flux adjustment	27.5–28.1	26.3–27.0	Isopycnal layer thickness diffusion (Gent et al., 1995) and isopycnal diffusion (Cox, 1987) with weak background horizontal Laplacian diffusion	Turbulence closure scheme of Noh and Kim (1999)
Meteorological Institute of the University of Bonn ECHAM4 + HOPE G	MIUB ECHO G	Heat and water flux adjustment outside sea ice region	27.9–28.4	26.0–26.5	Harmonic and shear-dependent eddy diffusion of tracers	
Max Planck Institute for Meteorology	MPI ECHAM5	No flux adjustment	27.3–28.1	26.1–26.7	Gent et al. (1995) and Griffies (1998)	Vertical eddy viscosity and diffusion: Richardson-number independent scheme of Pacanowski and Philander (1981). Wind stirring at surface proportional to (10 m wind speed)^3 and decays exponentially with depth
Meteorological Research Institute, Japan Meteorological Agency, Japan coupled global climate model	MRI CGCM2.3.2A	Monthly flux adjustment for heat, water, momentum (only 12°S–12°N)	27.4–28.3	26.1–27.0	Laplacian-type horizontal diffusion + GM parameterization (Gent and McWilliams, 1990)	Turbulent closure level 2 (Mellor and Yamada, 1974; Mellor and Durbin, 1975)
UK Met Office Hadley Centre for Climate Prediction and Research coupled model	UKMO HADCM3	Only for freshwater imbalance due to snow accumulating over ice sheets	27.2–28.4	26.2–26.6	Gent and McWilliams (1990) with variable thickness diffusion parameterization (Wright, 1997; Visbeck et al., 1997)	Kraus and Turner (1967), K-theory scheme (Pacanowski and Philander, 1981) for momentum
UK Met Office Hadley Centre for Climate Prediction and Research Global Environmental Model	UKMO HADGEM1	Only for freshwater imbalance due to snow accumulating over ice sheets	27.3–28.2	25.8–26.7	Isopycnal diffusivity with constant value of 500 m^2/s using Griffies et al. (1998) scheme. Adiabatic mixing scheme in skew flux form (Gent and McWilliams 1990; Griffies, 1998) spatially and temporally varying coefficient (Visbeck et al., 1997; Roberts et al., 2004)	Kraus and Turner (1967), K-theory scheme (Pacanowski and Philander, 1981) for momentum

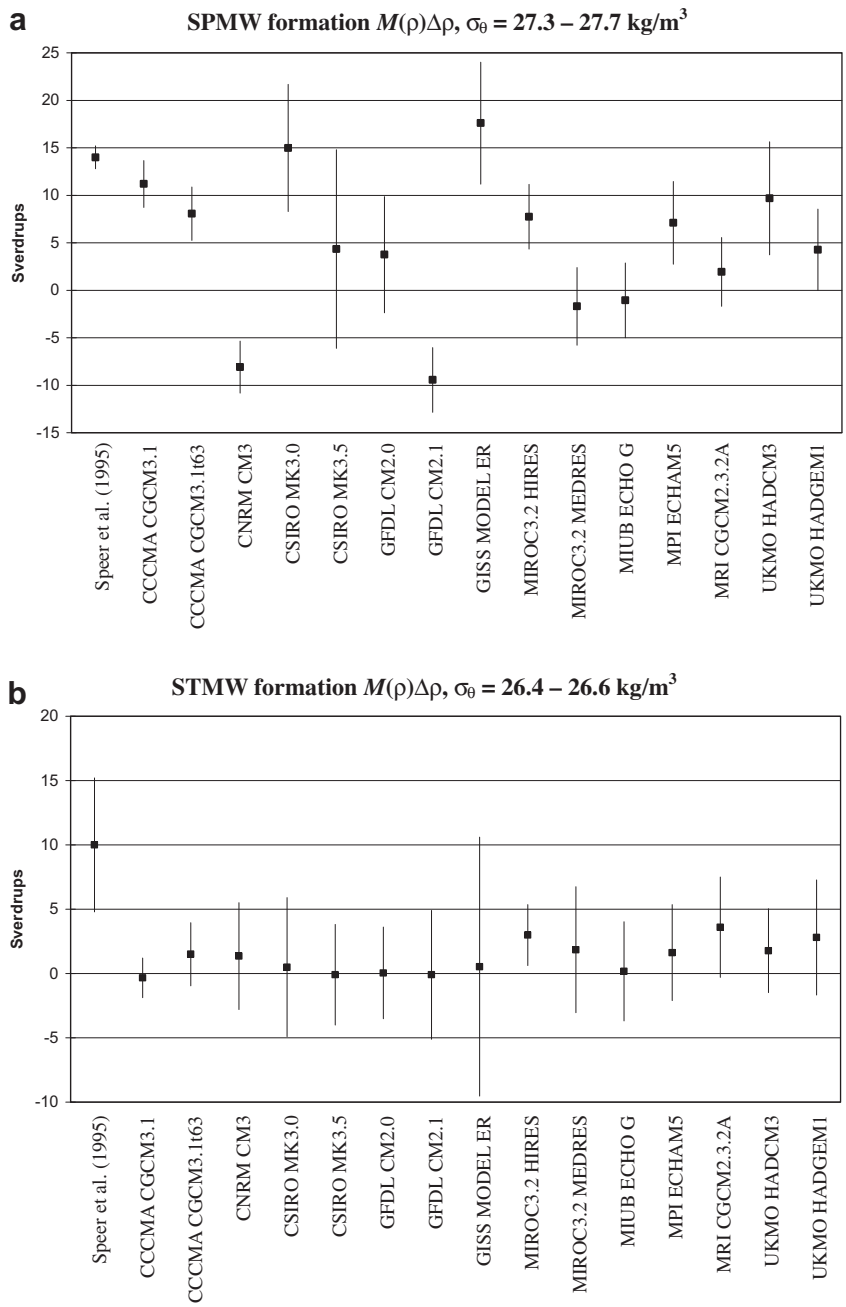

Fig. 1. (a) SPMW formation rates ($M(\rho)\Delta\rho$) in Sverdrups for σ_θ = 27.3–27.7 kg/m^3. Values are means; error bars give ranges of one standard deviation. (b) STMW formation rates ($M(\rho)\Delta\rho$) in Sverdrups for σ_θ = 26.3–26.6 kg/m^3. Values are means; error bars give ranges of one standard deviation.

For STMW, the mode water formation rate, $M(\rho)\Delta\rho$, calculation using a σ_θ range of 26.4–26.6 kg/m^3 produces mean values near zero with wide error ranges (Fig. 1b). The water mass transformation, $F(\rho)$, curves in Fig. 2 explain this result as well; for some models there is no clear separation in water types formed and no clear region of negative gradient, resulting in extremely small formation rates. For other models one may diagnose formation of a secondary water mass, but it falls in a density class different from σ_θ = 26.4 to 26.6 kg/m^3; for several models (e.g. CCCMA CGCM3.1, MPI ECHAM5) the density class σ_θ = 26.4–26.6 kg/m^3 falls in the transformation rate minimum between formation of SPMW and the lighter class of water. For one extreme case (GISS MODEL E R) there is no secondary water mass formation at all.

Fig. 3 shows contours of winter buoyancy fluxes for data and each model. The observational fluxes were calculated using NODC (Levitus) World Ocean Atlas Data 1998 temperature and salinity data (Monterey and Levitus, 1997), and surface fluxes from the National Oceanography Centre, Southampton version 2.0 dataset (Berry and Kent, 2009)) and for each model. Each plot also shows coloured regions defined by the published density classes for SPMW and STMW as they occur in the data and each model for the same winter, defined as January-February-March (JFM), period. Regions with large positive buoyancy fluxes overlaying the appropriate σ_θ value may be interpreted as the outcropping window for the particular water type.

Observed positive buoyancy fluxes (representing density increase) over the outcrop associated with SPMW are found across the extent of the subpolar gyre and the Norwegian Sea (Fig. 3); buoyancy flux values vary from 5 to 9 mg/m^2/s with the highest values occurring south of Iceland in the vicinity of the North Atlantic Current (NAC). The various models each show a sizeable sub-polar region with buoyancy fluxes in the range of 5–12 mg/m^2/s resulting in the formation of that model's densest water mass.

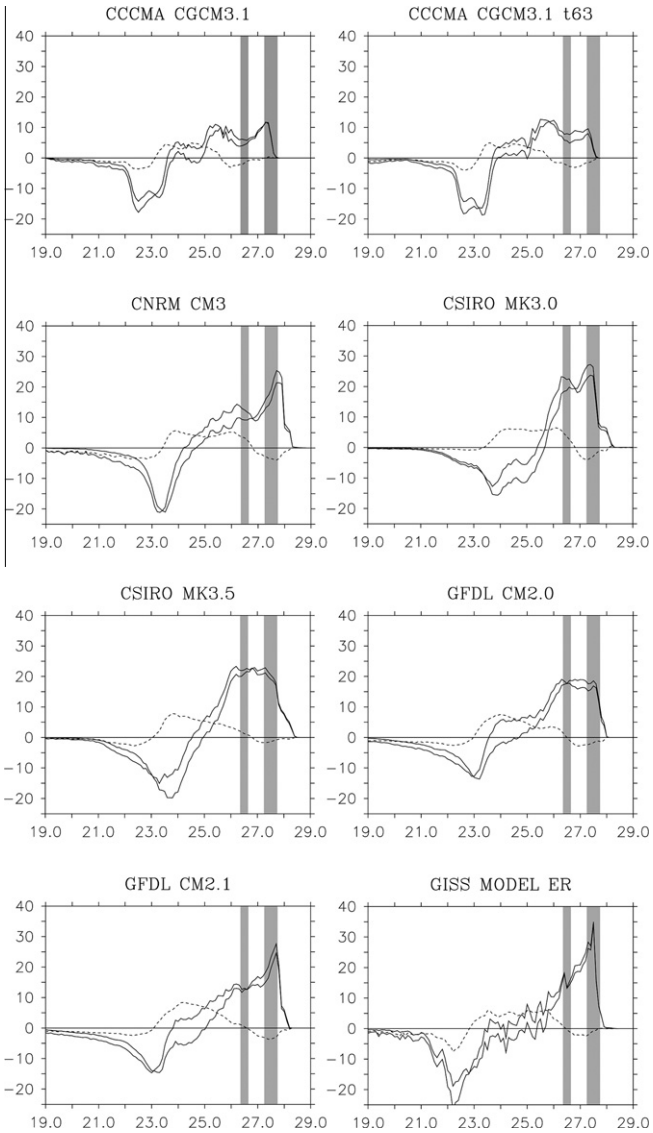

Fig. 2. Water mass transformation $F(\rho)$ curves, in Sverdrups for different σ_θ. Thin line is transformation due to heat fluxes; dashed line is transformation due to water fluxes, thick line is total transformation rate. Grey shaded areas highlight the density classes of STMW and SPMW in the ocean: $\sigma_\theta = 26.4–26.6$ kg/m^3 and $\sigma_\theta = 27.3–27.7$ kg/m^3.

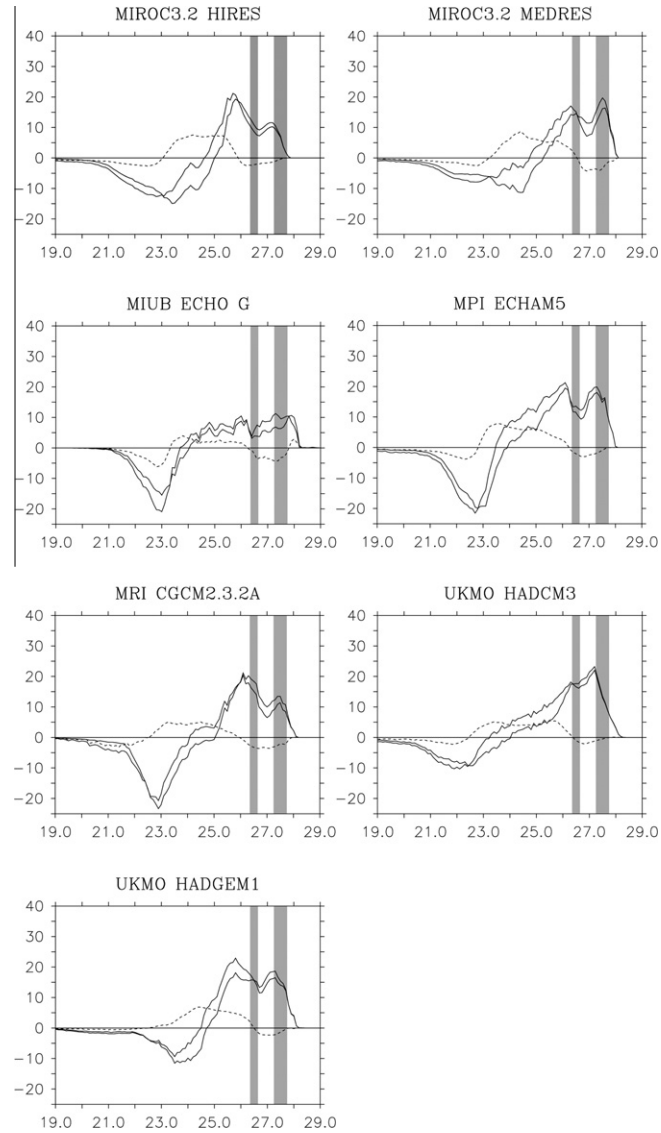

Fig. 2 (*continued*)

For those models which form a water type more dense than the observed SPMW, using the standard SPMW density classes as an outcropping mask surrounds but misses the formation regions. For example, Fig. 3's plot of CNRM CM3 buoyancy fluxes shows a large gap in the subpolar North Atlantic and Labrador Sea regions surrounded by the $\sigma_\theta = 27.3–27.7$ kg/m^3 outcropping. CNRM CM3 forms water denser than observed SPMW within that subpolar North Atlantic and Labrador Sea region (Fig. 2).

Examination of the STMW σ_θ ranges (Fig. 3) for the data show large positive buoyancy fluxes intersecting $\sigma_\theta = 26.4–26.6$ to the south of the Gulf Stream extension. Buoyancy flux values vary from 10 to 16 mg/m^2/s in this small region. In the models, the buoyancy fluxes at these density classes vary widely, as do the locations of the intersecting σ_θ region. Some models (CCCMA CGCM3.1, CCCMA CGCM3.1 t63) show only small regions to the south of the Gulf Stream where these σ_θ classes overlay the high buoyancy flux associated with Gulf Stream heat transfers. Other models (GFDL CM2.0, GFDL CM2.1) show considerable buoyancy flux in the Gulf Stream region, while UKMO HADGEM1 shows little buoyancy flux in the Gulf Stream region but more in the North Atlantic drift region.

For this intermediate water type, each model appears to manage the combination of surface densities and buoyancy fluxes sufficiently differently as to produce the widely varying STMW formation rates, $M(\rho)\Delta\rho$, seen in Fig. 1b.

3.2. WMTR comparisons: model-specific σ_θ ranges

From the water mass transformation, $F(\rho)$, plots in Fig. 2 it was apparent that many (not all) models form two separate water masses, although density classes formed do not necessarily match those observed in nature. To examine the hypothesis that a model might be forming mode waters, simply at a different density class, we needed to identify density classes being formed for each model. We examined monthly (January, February, and March) and winter season (JFM) water-mass transformation $F(\rho)$ and formation per unit density, $M(\rho) = -dF/d\rho$, curves and identified density ranges with negative WMTR gradient (positive formation), for both SPMW and STMW, for each model. All the models formed a densest water mass; hence they all form a water mass analogous to SPMW. Their treatment of the phenomena producing the intermediate water

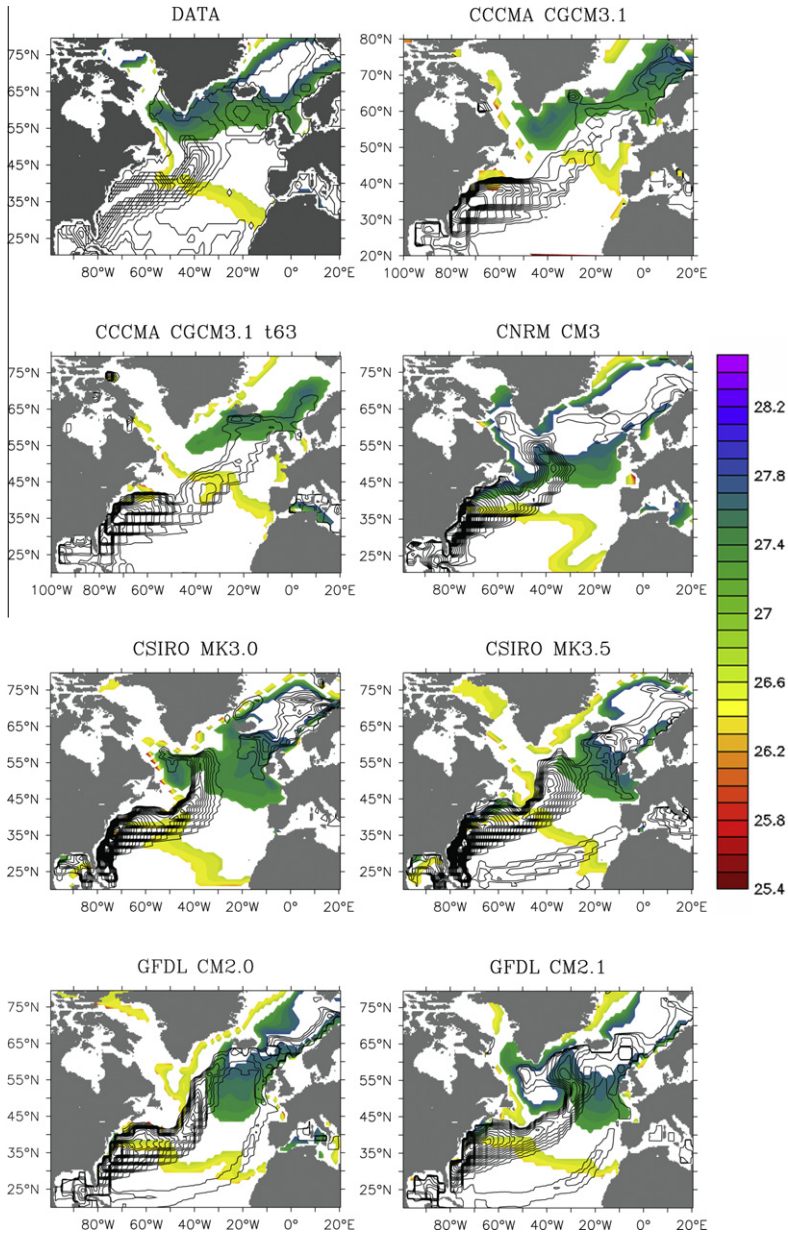

Fig. 3. JFM buoyancy flux (total heat and fresh water, mg/m^2/s) through the surface, contoured each 1 mg/m^2/s from 5 mg/m^2/s upward. Regions with JFM surface σ_θ = 27.3–27.7 (SPMW) and σ_θ = 26.4–26.6 (STMW) are shown in colour.

mass were more variable: these models can be sorted into two groups based on their treatment of STMW formation. One set of cases showed realistic behaviour with clear STMW density classes formed; the other set of cases showed unrealistic STMW formation.

Fig. 4 compares a realistic and unrealistic example of winter season water-mass transformation, $F(\rho)$, and formation per unit density, $M(\rho) = -dF/d\rho$, curves, representative of the two groups. Those models that have a distinct (if small) secondary region of negative slope in WMTR (Fig. 2), resulting in positive STMW formation, show a corresponding distinct peak in winter formation rates. Fig. 4 shows the overall winter, and winter monthly transformation, $F(\rho)$, (Fig. 4a) and formation per unit density, $M(\rho) = -dF/d\rho$, (Fig. 4b) rates for MIROC3.2 HIRES, producing a STMW density range of 25.7–26.7. As the season progresses from January to February to March, the monthly maximum of formation per unit density, $M(\rho) = -dF/d\rho$, moves to denser σ_θ classes as each subsequent month's cooling and mixing acts to increase the density of the water classes formed the previous month until springtime heating caps the vertical mixing. Cerovecki et al. (2011) first noted this progressive density increase in time when examining Southern Ocean WMTRs. For those models with this type of STMW formation (CCCMA CGCM3.1, CCCMA CGCM3.1 t63, CNRM CM3, CSIRO MK3.0, MIROC3.2 HIRES, MIROC3.2 MEDRES, MIUB ECHO G, MPI ECHAM5, MRI CGCM2.3.2A, UKMO HADGEM1) the σ_θ choice was consistent whether using seasonal or annual WMTR curves; in other words, the winter seasonal signal dominated the annual signal.

Those models having a broad, diffuse or indiscernible secondary peak in WMTR (Fig. 2) displayed a different seasonal/monthly STMW transformation, $F(\rho)$, and formation per unit density, $M(\rho) = -dF/d\rho$, behaviour. Fig. 4 shows the overall winter, and winter monthly, transformation (Fig. 4c) and formation (Fig. 4d) rates for CSIRO MK3.5. Note that rather than one distinct range

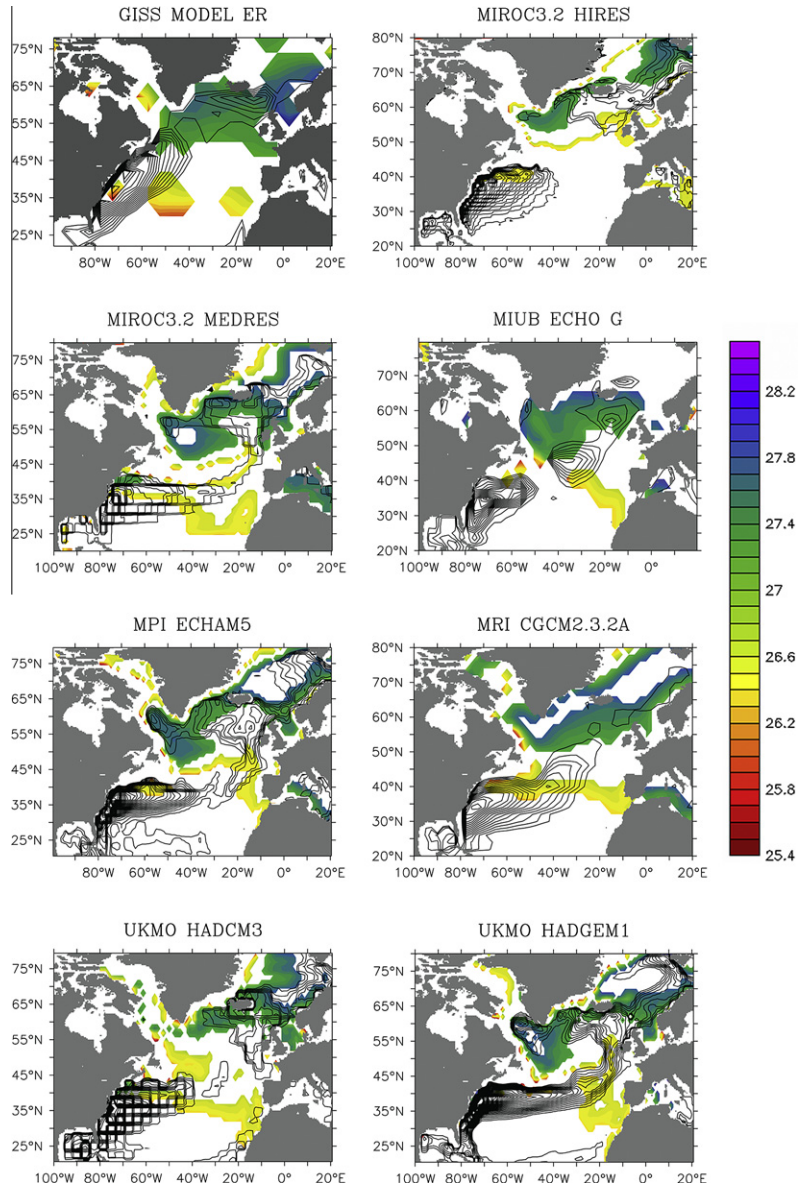

Fig. 3 (*continued*)

of densities for STMW, the formation rate per unit density, $M(\rho) = -dF/d\rho$, shows several small, narrow peaks in successive density ranges progressing toward identifiable SPMW. Identifying any one peak with STMW and excluding the others appeared to exclude important geographic formation regions off the North American coast; additionally, in those models with multiple ensemble members, there was little run-to-run consistency in formation per unit density sub-classes. For these models with ill-behaved STMW formation (CSIRO MK3.5, GFDL CM2.0, GFDL CM2.1, GISS MODEL E R, UKMO HADCM3) σ_θ choices were determined by plotting buoyancy fluxes through the σ_θ ranges with positive formation rates and selecting the σ_θ range in the Gulf Stream zone. We recognise that the results may not be optimal; however these model biases preclude a substantially better approach.

Using these methods, density classes were determined at which each model was forming water types; density classes formed for each model are given in Table 1. In many cases this technique resulted in a broader range of density classes for STMW than documented, even for well-behaved models. Fig. 5 shows formation rate, $M(\rho)\Delta\rho$, in Sverdrups, for each model compared with the mode water formation data of Speer et al. (1995); models with broad, diffuse, or indiscernible secondary peak in WMTR $F(\rho)$ are highlighted with triangular data points. Particularly for STMW, these formation rate, $M(\rho)\Delta\rho$, results with the broader σ_θ ranges more meaningfully matched natural quantities: while considerable variation remains in amounts formed, the means are no longer near zero and are of the same order of magnitude as the data.

While no firm correlation exists, those models forming smaller amounts of STMW have a weak tendency to form larger amounts of SPMW (CNRM CM3, CSIRO MK3.0, CSIRO MK3.5, GFDL CM2.1, and GISS MODEL E R, UKMO HADCM3) and vice versa (CCCM CGCM3.1, CCCMA CGCM3.1t63, MIROC3.2 HIRES, MIROC3.2 MEDRES, MIUB ECHO G, MPI ECHAM5, MRI CGCM2.3.2A, UKMO HADGEM1). The latter group (more STMW formation, less SPMW formation) shows better agreement with the data of Speer et al. (1995), particularly for SPMW.

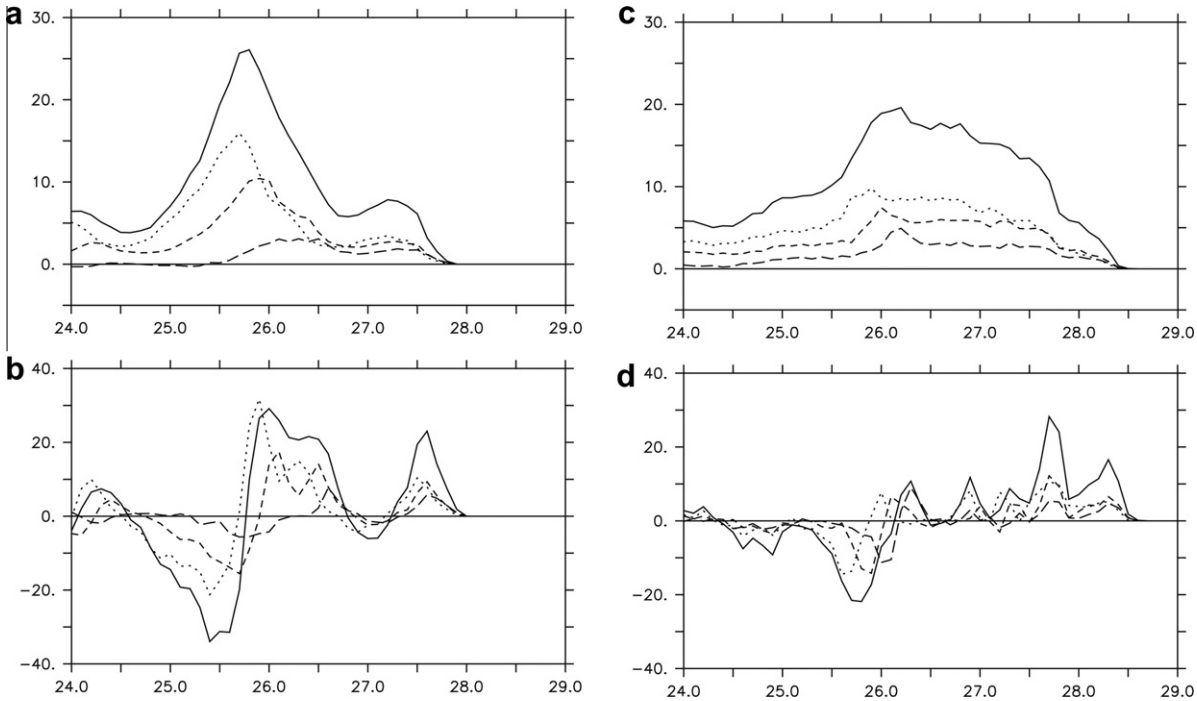

Fig. 4. Transformation ($F(\rho)$) rates (Sv) and formation per unit density ($M = -dF/d\rho$) rates vs. σ_θ for two models. (a) MIROC3.2 HIRES transformation rate; (b) MIROC3.2 HIRES formation per unit density rate; (c) CSIRO MK3.5 transformation rate, (d) CSIRO MK3.5 formation per unit density rate. Short-dashed lines are January, medium-dashed lines are February, long-dashed lines are March, and bold lines are JFM total.

The geographic locations of surface fluxes relative to both the density classes being formed and the mixed layer depths provided some insight into the variation in model water mass formation rates, $M(\rho)\Delta\rho$. Fig. 6 shows the winter buoyancy fluxes intersecting JFM σ_θ regions defined by each model's WMTR calculation (per Fig. 2 and Table 1), with the same data comparison as in Fig. 3. Notably the regions of SPMW formation now include the expected formation zones with areas of ample buoyancy flux out of the ocean (no excluded zones where yet-denser water is being formed). Again, in these graphics the regions with large positive buoyancy fluxes intersecting the appropriate σ_θ range may be interpreted as the outcropping window of the particular water type.

The regions of STMW formation are more variable with these wider STMW σ_θ definitions but still include much broader areas with sizeable buoyancy flux, particularly in the Gulf Stream separation and recirculation zone (whether or not an individual model showed recirculation). In particular, the broad fan of high buoyancy flux off the North American coast (values up to 20 mg/m^2/s) resulted in substantial STMW formation rates, $M(\rho)\Delta\rho$, (Fig. 5b) and the pronounced transformation rate $F(\rho)$ peak (Fig. 2) (CCCMA CGCM3.1, CCCMA CGCM3.1 t63, MIROC3.2 HIRES, MRI CGCM2.3.2A). Alternatively, models with a smaller area of buoyancy flux through the σ_θ classes produced smaller amounts of STMW (CNRM CM3, CSIRO MK3.0, MIUB ECHO G). MIROC3.2 MEDRES, MPI ECHAM5, and UKMO HADGEM1 represent an intermediate group of models with relatively small areas of buoyancy flux through the σ_θ classes but moderate amounts of STMW formation $M(\rho)\Delta\rho$; from Fig. 6 we can see that these formation amounts might be biased high by an extended zone of positive buoyancy flux following the storm track north through the eastern Atlantic.

The breadth of STMW σ_θ classes identified by this technique may be unrealistic even for well-behaved models, but given the strong model σ_θ gradients in the Gulf Stream/northwest Sargasso region, this broad range of σ_θ classes permitted a sufficient overlap area with the strong buoyancy fluxes to accumulate the more realistic STMW formation rates, $M(\rho)\Delta\rho$. Narrower breadth of σ_θ ranges would again have resulted in low STMW formation rates.

Temperature–salinity (T–S) diagrams were used to examine specific properties of the model mode waters corresponding to the selected σ_θ classes. Fig. 7 shows surface T–S in the density classes produced by each model for JFM. Values are restricted to within 25°–45°N, 45°–80°W and model STMW σ_θ ranges, and 55°–80°N, 20°E–60°W and model SPMW σ_θ ranges. These regions were selected as they encompass the locations of large water mass formation. T–S points from the NODC (Levitus) World Ocean Atlas Data 1998 in the observed STMW and SPMW σ_θ ranges for JFM were included to provide a fidelity check (Monterey and Levitus, 1997). The data show a clear water-mass separation between the warmer, saltier STMW and the cooler, fresher North Atlantic Slope Waters and Shelf waters (presumably in the vicinity of the Grand Banks) in the density classes σ_θ = 26.4–26.6 kg/m^3. SPMW waters are identified in the σ_θ = 27.3–27.8 kg/m^3 range.

Note that the σ_θ choices appropriate to each model result in significant temperature and salinity differences from data for these water masses. The T–S diagrams show model SPMW temperatures to be often too cold, clustering near freezing point. Some of the models have salinities that are too high relative to observations. Models with SPMW values that are too saline (Fig. 7) form corresponding excessively dense SPMW as seen in Fig. 2. For STMW, the T–S diagrams demonstrate the broader σ_θ ranges chosen by the WMTR method and show some of the models having too-light water and/or no clear separation between water types as seen in the data for these density classes. GFDL CM2.1 is the most realistic in these density classes. Looking at the model-specific density classes in the 17–18 °C range, model density errors in producing STMW arise from both temperature and salinity errors. These errors reflect the multiple modelling problems that could result in erroneous STMW formation, to be discussed below. While model diagnostics and scaling

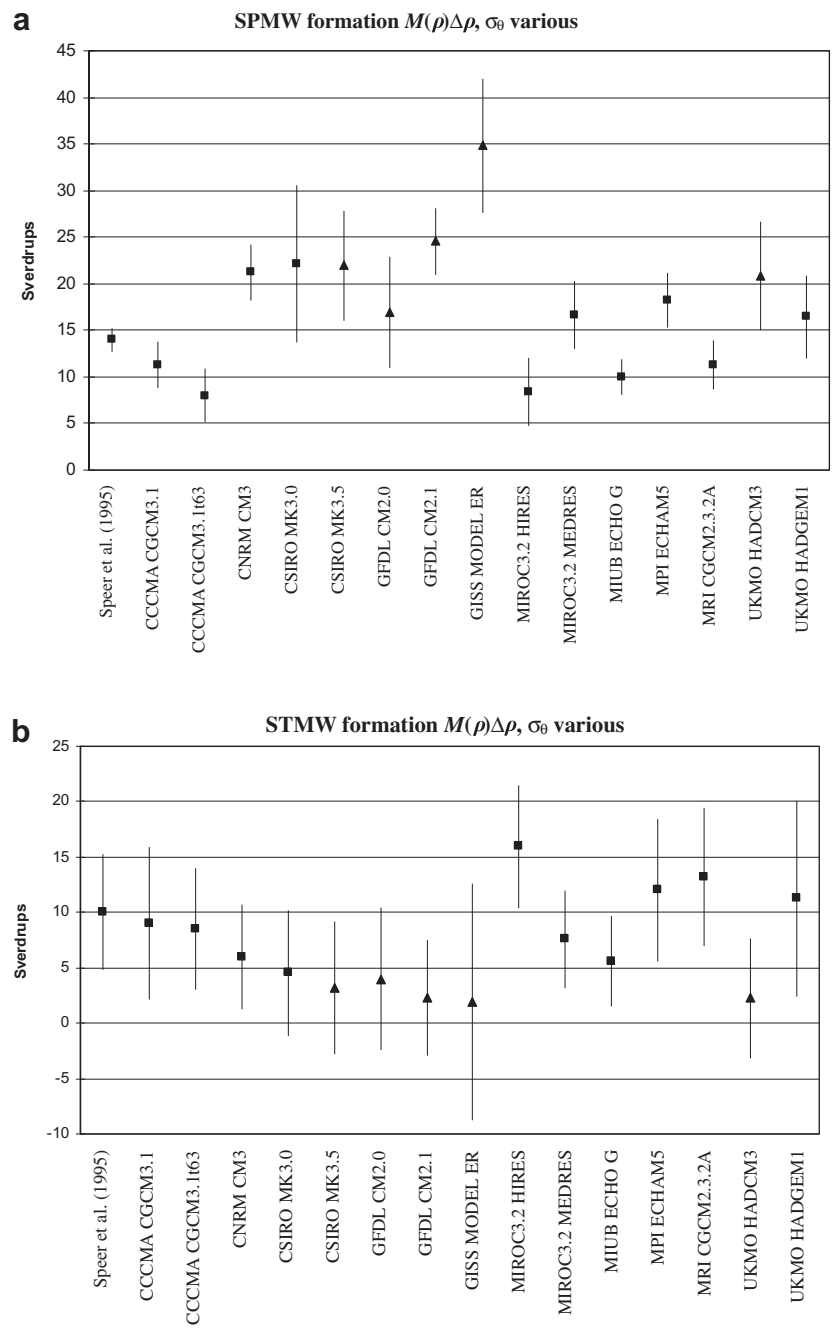

Fig. 5. (a) SPMW formation rates ($M(\rho)\Delta\rho$) in Sverdrups for σ_θ taking various values chosen for each model to capture the dense water formation for that model. Values are means; error bars give ranges of one standard deviation. Square data symbols indicate those models with a distinct (if small) secondary WMTR peak corresponding to STMW formation. Triangular data symbols indicate those models with broad, diffuse, or indiscernible STMW formation $F(\rho)$ peak. (b) STMW formation rates ($M(\rho)\Delta\rho$) in Sverdrups for σ_θ taking various values chosen for each model to capture the dense water formation for that model. Values are means; error bars give ranges of one standard deviation. Square data symbols indicate those models with a distinct (if small) secondary WMTR peak corresponding to STMW formation. Triangular data symbols indicate those models with broad, diffuse, or indiscernible STMW formation $F(\rho)$ peak.

analyses have suggested that surface fluxes dominate entrainment and lateral mixing in changing water mass density (Large and Nurser, 2001), the entrainment and lateral mixing are not insignificant (Nurser et al., 1999). Differences in various models' treatment of these processes from model to model, and from model to data, could cause the wide range of temperature and salinity properties for STMW seen for many models in Fig. 7 as well as the differences in transformation rates, $F(\rho)$, and formation rates, $M(\rho)\Delta\rho$, seen for each model.

4. Factors governing model mode water formation

4.1. SPMW formation

All the models formed a most-dense water mass identified as SPMW; aside from quantity formed, the greatest issue seemed to be positioning of the formation region. Fig. 6 shows buoyancy flux through outcropping areas defined by the density classes of SPMW for each model (outcropping areas with blue σ_θ contours); one

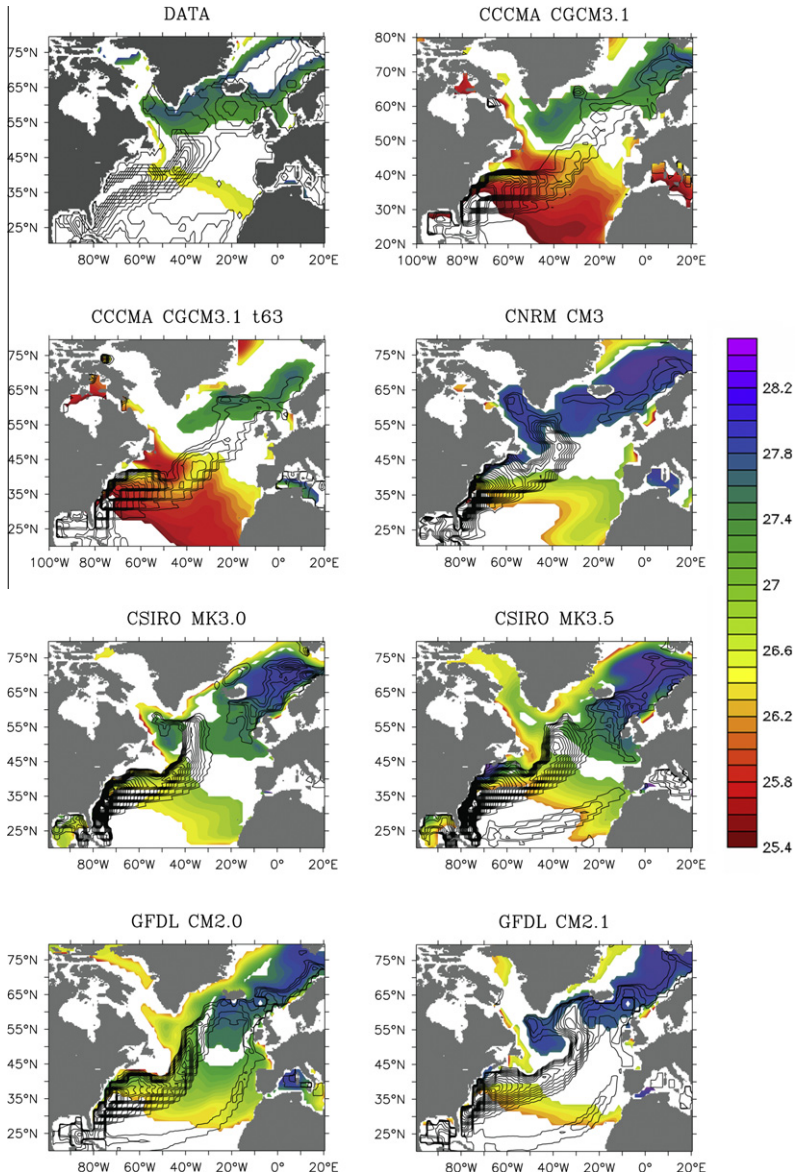

Fig. 6. JFM buoyancy flux (total heat and fresh water, mg/m^2/s) through the surface, contoured each 1 mg/m^2/s upward from 5 mg/m^2/s. Regions with JFM surface σ_θ chosen per Table 1 are shown in colour.

notable difference is between models with significant SPMW formation in the Labrador Sea (CCCMA CGCM3.1, CNRM CM3, GFDL CM2.1, GISS MODEL E R, MIROC3.2 HIRES, MIROC3.2 MEDRES, MIUB ECHO G, MPI ECHAM 5, MRI CGCM2.3.2A, UKMO HADCM3, UKMO HADGEM1) and models with SPMW formation in the region south of Iceland and west of Great Britain (CSIRO MK3.0, CSIRO MK3.5, GFDL CM2.0). These latter models may have issues positioning the warm, light advection of the North Atlantic Drift, permitting the preconditioned density classes associated with SPMW to extend southward in the eastern North Atlantic.

An example of contrasting SPMW formation is seen in the MIROC3.2 HIRES and CSIRO MK3.0 models. Both models exhibit SPMW formation in the Labrador Sea (Figs. 8 and 9), however only a small region of dense water is formed there in CSIRO MK3.0; the largest amount formed west of Great Britain (Fig. 9). MIROC3.2 HIRES shows the SPMW outcropping σ_θ classes co-located with the deepest mixed layers in the Labrador, Irminger, and Norwegian Seas (Fig. 8). While the outcropping region was not one of maximum buoyancy flux, the flux was sufficient for ample SPMW formation. The surface currents in Fig. 8 for MIROC3.2 HIRES show the North Atlantic Drift (NAD) extending northeastward and then northward to the west of Great Britain, consistent with the large buoyancy flux between Iceland and Great Britain. The SPMW outcropping regions, however, more closely match mixed layer deepening than heat flux. In contrast, CSIRO MK3.0 (Fig. 9) shows southeast and eastward currents in this region except to the south of Iceland where weak northeast flow is found. These anomalous currents advect cold subpolar waters into the eastern Atlantic producing denser surface waters than those resulting from the warm southern waters. This causes a bias in convection sites as evidenced by the excessively deep mixed layers off Great Britain. The outcropping σ_θ classes for SPMW coincide with the deepest mixed layers (greater than 1300 m west of Britain) and strong buoyancy flux in the subpolar region.

It is reasonable to attribute this bias in SPMW formation in the eastern Atlantic to the incorrect setup of the subpolar ocean circulation by the atmospheric winds. The mis-positioning of the North Atlantic Drift and the unrealistic subpolar surface flows wrongly

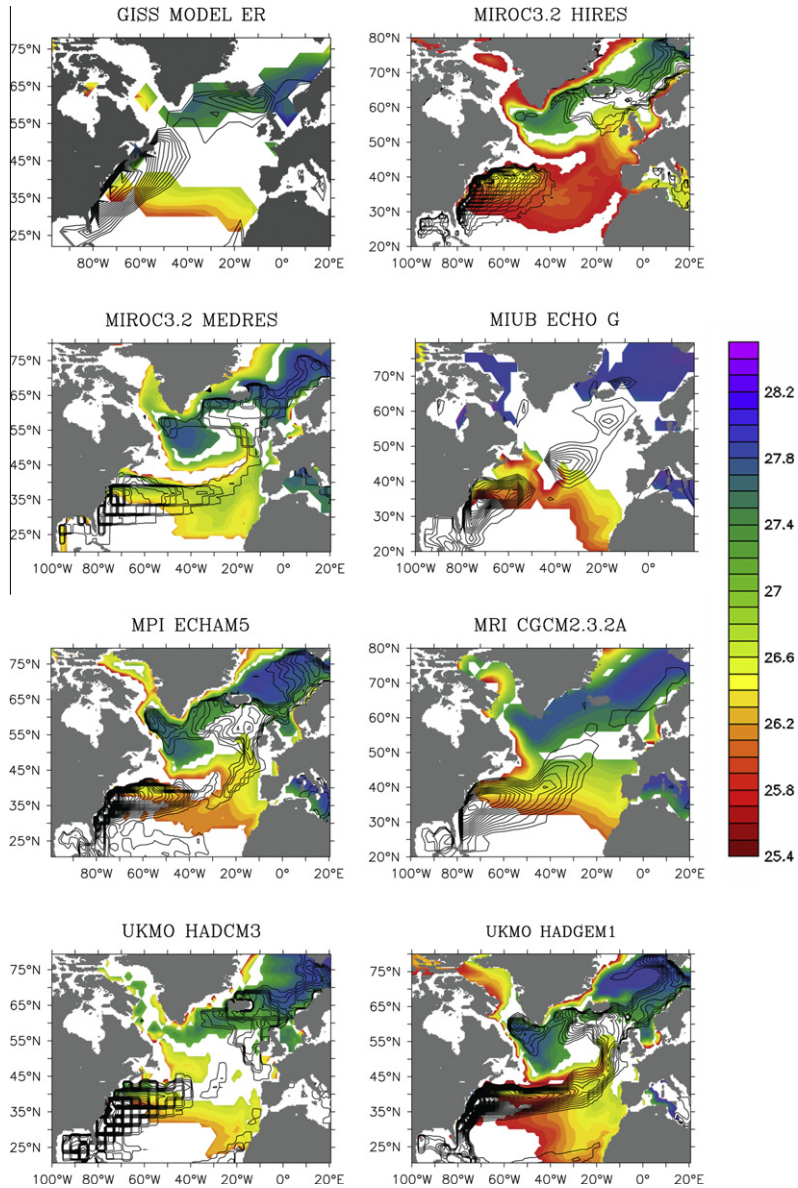

Fig. 6 (*continued*)

precondition the water in the eastern Atlantic, thus shifting convection sites that produce unrealistically deep mixed layers. An examination of the de Boyer-Montégut mixed layer climatology (De Boyer Montégut et al., 2004) shows winter mixed layer depths in the eastern North Atlantic to be around 100–300 m deep, rather than CSIRO MK3.0's mixed layer depth of over 600 m deep. The vertical mixing parameterization may further exacerbate this deepening. CSIRO MK3.0 uses an integer power vertical mixing scheme (Wilson, 2000, 2002) based on that of Pacanowski and Philander (1981). The latter scheme is tuned for the tropics where it produces a too-diffuse equatorial thermocline.

Alternatively, as the ocean and atmosphere models are coupled, one can view the cause–effect sequence of wind biases and mixed layer deepening in the opposite direction. The East Atlantic deep mixed layer, being slightly cooler at the surface, would release less heat to the atmosphere. The resulting cool lower troposphere would deflect winds cyclonically to the south around the cooler region, leading to the wind deflection seen in Fig. 9. Indeed, CSIRO MK3.0 winter surface temperatures (not shown) have a pronounced warm pool in the western central North Atlantic south of Greenland, with slightly cooler temperatures west of Great Britain. We note that these two mechanisms could act on each other with positive feedback, which could lead to the coupled models evolving to these two extremes of mode water formation: in the eastern North Atlantic vs. toward the Labrador Sea.

We may expect these location differences in SPMW formation to have a significant effect on the simulated Atlantic MOC. Not all models archived the AMOC, and some models blanked the Nordic Seas region from the fields they archived; however, those archived meridional overturning streamfunction fields shown in Figs. 10 and 11 confirm features noted in Figs. 8 and 9. To continue the comparison of MIROC3.2 HIRES and CSIRO MK3.0, the AMOC from these two models are shown in Fig. 10. MIROC3.2 HIRES (Fig. 10a) shows a pronounced overturning cell in the upper 3000 m of the water column that has a maximum strength of more than 12 Sv centred in about 1000 m depth at about 42°N. About 4 Sv of this upper branch flows poleward into the upper Nordic Seas and then returns to the North Atlantic contributing to the downwelling arm that occurs to the north of 50°N. Its lower southward branch represents NADW. These flows are comparable to the

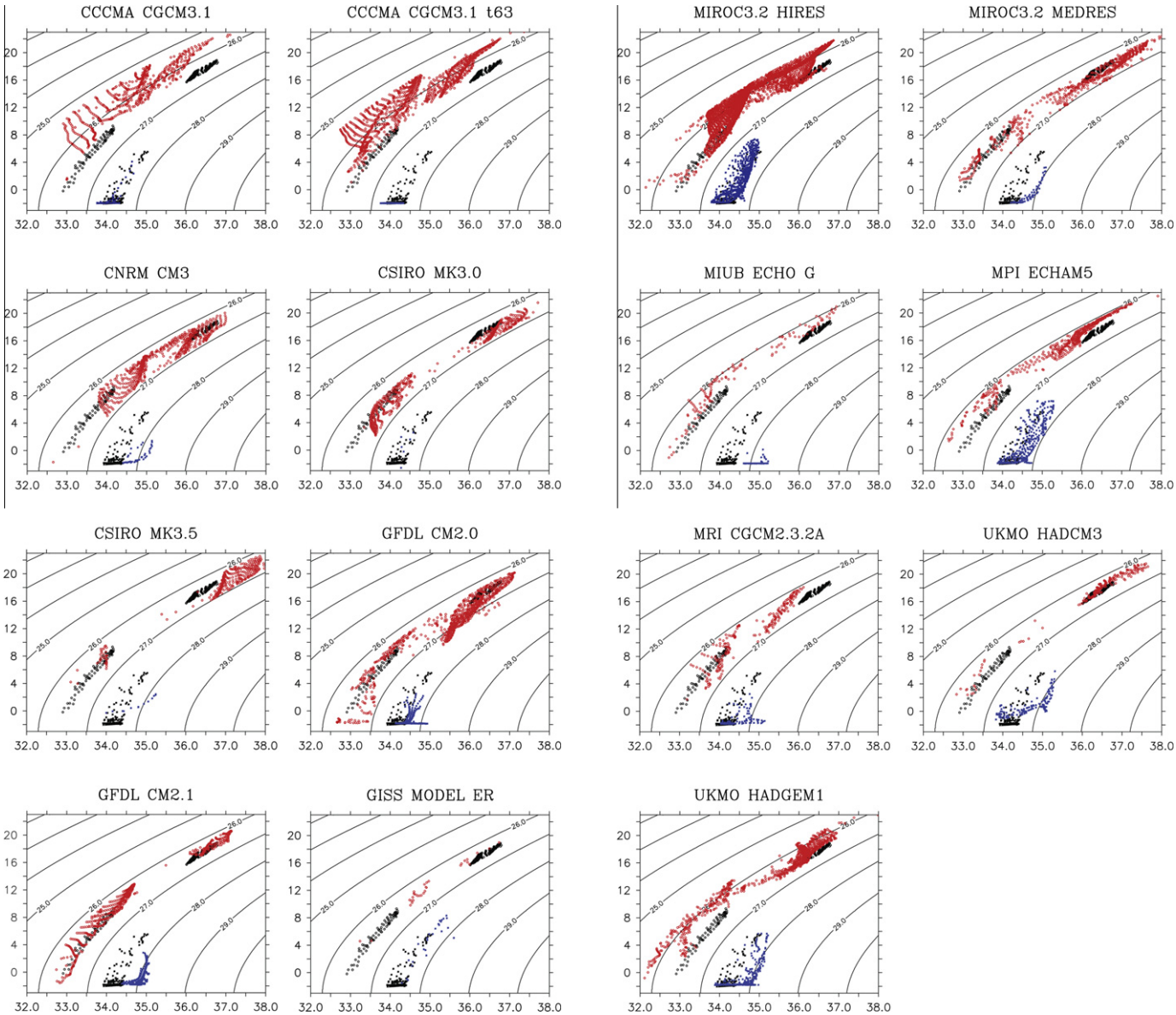

Fig. 7. T–S diagrams for the model mode waters. Red points represent JFM data within 25–45°N, 45–80°W and model STMW σ_θ; blue points represent JFM data within 55–80°N, 20°E-60°W and model SPMW σ_θ. Comparison data in black are JFM Levitus data with σ_θ = 26.4–26.6 kg/m^3, σ_θ = 27.3–27.8 kg/m^3.

Fig. 7 (*continued*)

inverse analysis results of Lumpkin and Speer (2007; their Table 2); the 40°N flow of 12 Sv is close to the low end of their values (16.3 ± 2.7 Sv) for 48°N and the Nordic Sea flow of 4 Sv is within their values (4.0 ± 0.7 Sv) for the Greenland–Iceland–Scotland ridges. Thus the MIROC3.2 HIRES MOC is on the low end of the data range while the Nordic Sea branch of the circulation is on the high end of the data range, consistent with the strong NAC over the Iceland-Faeroes Gap seen in Fig. 8.

In the upper ocean the CSIRO MK3.0 AMOC (Fig. 10b) shows a shallow wind-driven cell whose strength is about 6 Sv with equatorward surface flows between 30°N and 50°N. The pronounced cell below it has a maximum strength of more than 16 Sv at about 30°N in about 1000 m depth. All of this poleward flowing upper arm downwells north of 50° to form NADW; none of this upper limb enters the Nordic Seas. The 16 Sv MOC circulation is well within the range 16.3 ± 2.7 Sv of Lumpkin and Speer (2007) for 48°N, however the lack of a Nordic Sea branch disagrees with observations. The near-surface streamfunction is understood by looking at the flow in Fig. 9; the pronounced surface circulation from 30° to 50°N is due to the broad area of southeast currents in that latitude range. Additionally, the low streamfunction gradient near the surface of Fig. 10b from 55°N to 65°N is due to lack of strong flow northward over the ridge to supply the Nordic Sea branch of the MOC. Finally just to the north of the descending MOC limb, an additional 3 Sv from the sill latitudes are sinking from the near surface and merging with the MOC cell. This contribution is likely due to the East Greenland Current transporting very cold water into the subpolar North Atlantic over the Greenland–Iceland Gap (Fig. 9b).

Completeness being worth some redundancy, Fig. 11 shows MOC comparisons for these two models as well as other models grouped according to SPMW formation zone. The various models in Fig. 11a, representing those which formed SPMW in the Labrador Sea, have widely varying values of northward flow in the upper limb of the MOC, as well as differences in the flow north into the Nordic Seas. Their salient feature, however, is that they involve

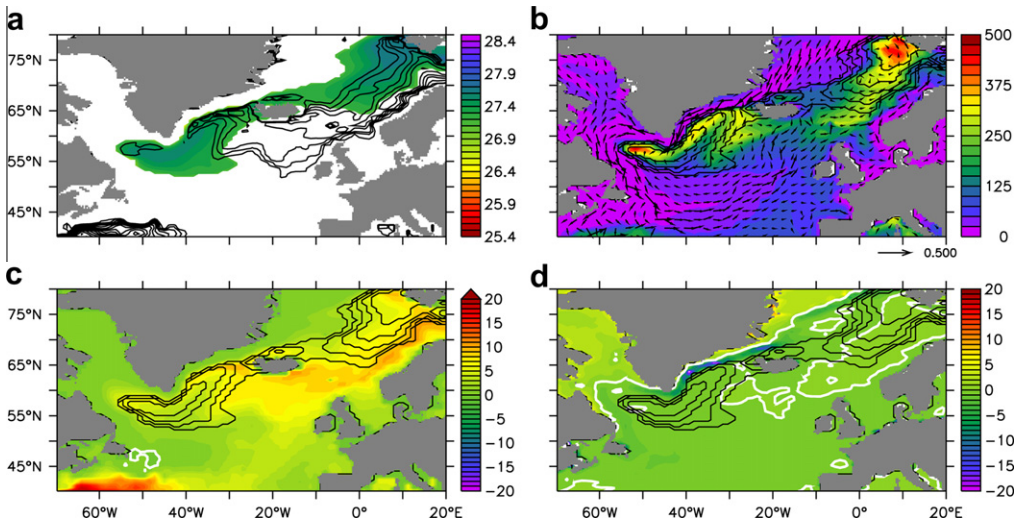

Fig. 8. MIROC3.2 HIRES. (a) JFM total buoyancy flux, contoured each 1 mg/m^2/s upward from 5 mg/m^2/s. Regions with surface σ_θ = 27.2–27.9 for SPMW are shown in colour. (b) JFM mixed layer depth (m) and February surface currents (m/s), with contours of surface σ_θ = 27.2–27.9. (c) JFM buoyancy flux due to heat (mg/m^2/s) out of the ocean, with contours of surface σ_θ = 27.2–27.9. (d) JFM buoyancy flux due to water/salt (mg/m^2/s) out of the ocean, with contours of surface σ_θ = 27.2–27.9. White contour is 0 of the flux.

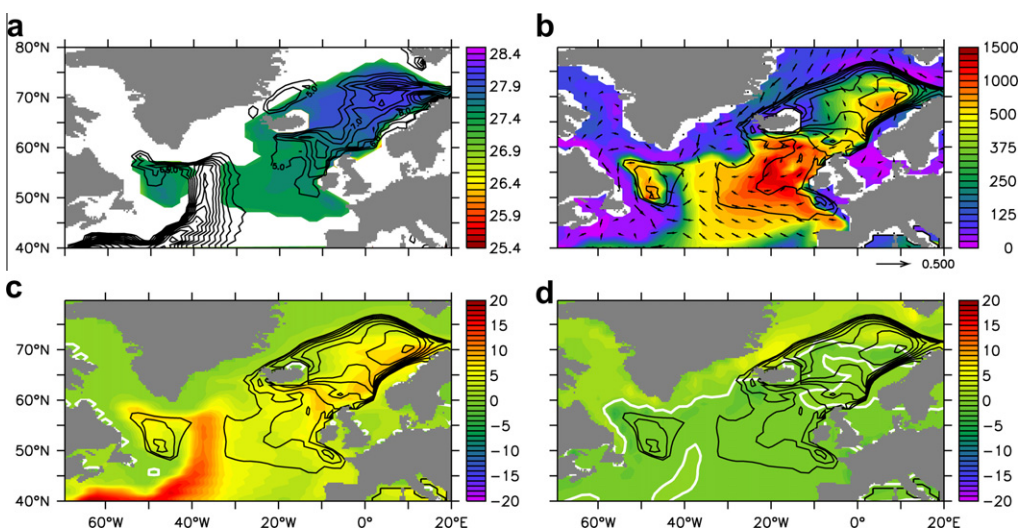

Fig. 9. CSIRO MK3.0. (a) JFM total buoyancy flux, contoured each 1 mg/m^2/s upward from 5 mg/m^2/s. Regions with surface σ_θ = 27.3–28.5 for SPMW are shown in colour. (b) JFM mixed layer depth (m, note nonlinear scale) and February surface currents (m/s), with contours of surface σ_θ = 27.3–28.5. (c) JFM buoyancy flux due to heat (mg/m^2/s) out of the ocean, with contours of surface σ_θ = 27.3–28.5. (d) JFM buoyancy flux due to water/salt (mg/m^2/s) out of the ocean, with contours of surface σ_θ = 27.3–28.5. White contour is 0 of the flux.

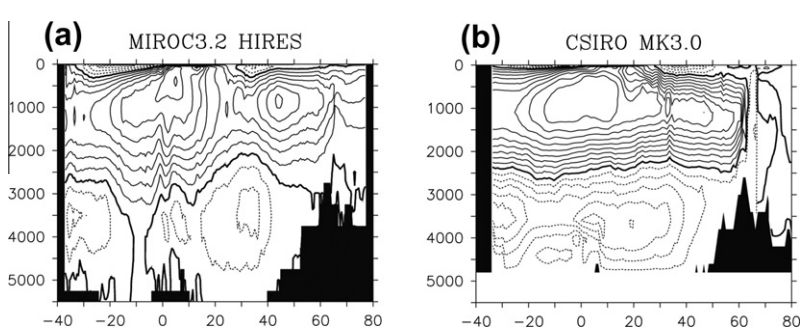

Fig. 10. Meridional overturning streamfunction for the North Atlantic (Sv). (a) MIROC3.2 HIRES. (b) CSIRO MK3.0. Contours are each 2 Sv.

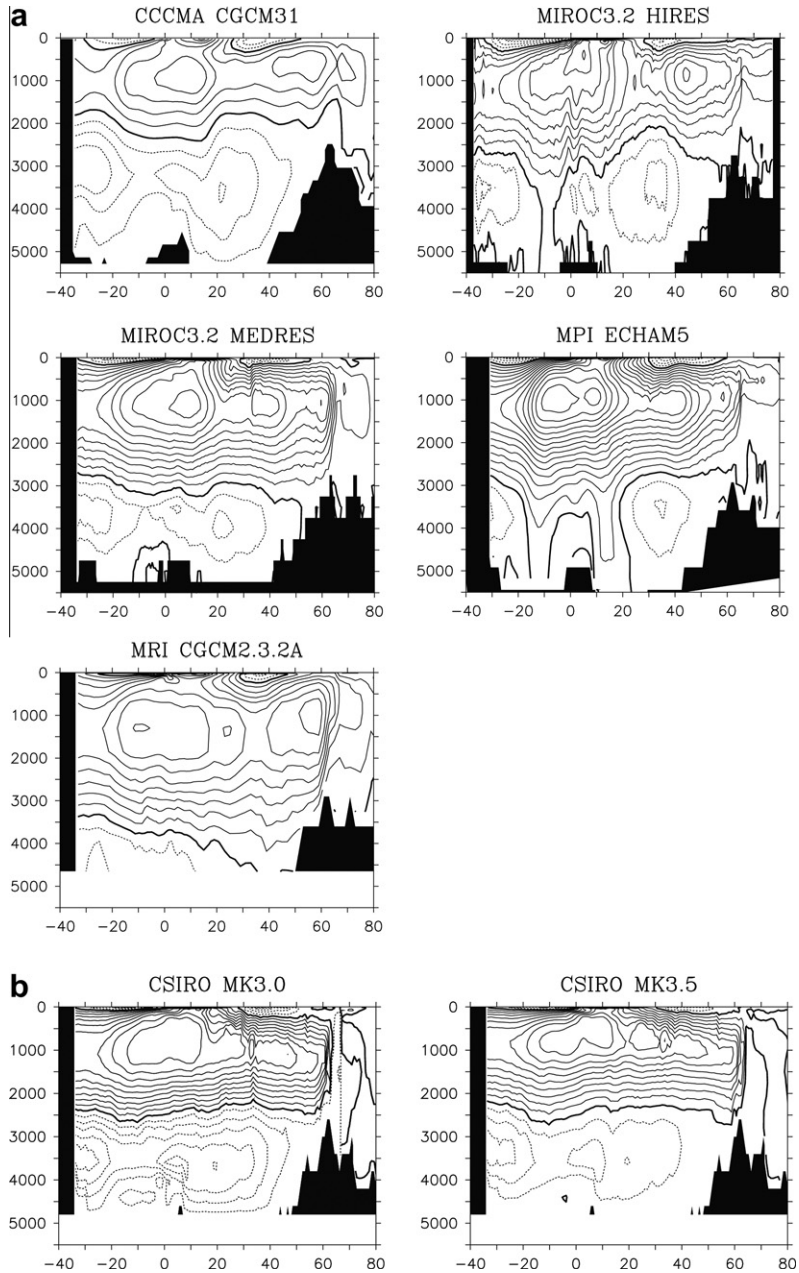

Fig. 11. (a) Meridional overturning streamfunction for the North Atlantic (Sv); models forming SPMW in the Labrador Sea. Contours are each 2 Sv. (b) Meridional overturning streamfunction for the North Atlantic (Sv); models forming SPMW west of Great Britain. Contours are each 2 Sv.

the Nordic Seas in the overturning circulation. In contrast, the smaller subset of models in Fig. 11b, representing those which formed SPMW in the eastern North Atlantic, show most or all of the northward flow of the upper limb of the MOC descending near 60°N with very little Nordic Sea involvement in the circulation. Other model-to-model differences in the MOC streamfunction fields would require a detailed parameter study to understand. However, with the caveat that the dataset for model-to-model comparison is small, other models appear to support the suggestion that SPMW formation in the region west of Great Britain blocks Nordic Sea involvement in the MOC.

4.2. STMW formation

The models displayed great variability in their ability to reproduce natural STMW formation. As mentioned above, Fig. 2 showed that some models formed water masses at two well-defined density ranges; some models formed water masses at two density ranges but the lighter one was poorly defined (shallow slope of $M(\rho) = -dF/d\rho$) or small in quantity; some models formed no clearly identifiable lighter water mass. Again, a weak pattern appeared (Fig. 5) that those models with the smallest amount of STMW formation (CNRM CM3, CSIRO MK3.0, CSIRO MK3.5, GFDL CM2.1, and GISS MODEL E R, UKMO HADCM3) had higher SPMW formation and vice versa (CCCM CGCM3.1, CCCMA CGCM3.1t63, MIROC3.2 HIRES, MIROC3.2 MEDRES, MIUB ECHO G, MPI ECHAM5, MRI CGCM2.3.2A, UKMO HADGEM1).

Contrasting STMW formation can be examined by comparing MIROC3.2 HIRES (Fig. 12) and CNRM CM3 (Fig. 13). Over its revised outcrop window MIROC3.2 HIRES produced about 16 Sv of STMW, just exceeding the upper limit of the observational range (10 ± 5 Sv). This model shows a pool of dense water associated with STMW offshore of the North American coast that is well aligned with the highest buoyancy fluxes out of the ocean. The pool

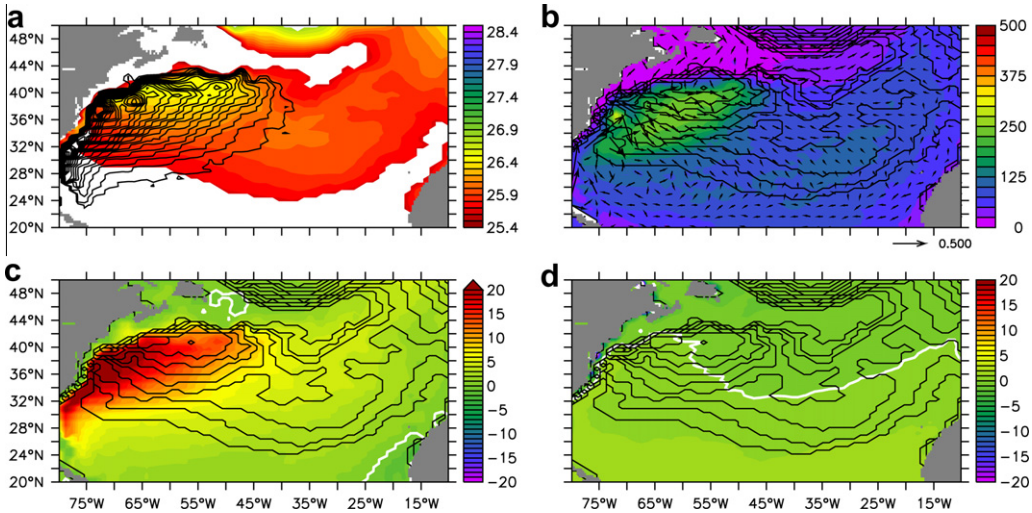

Fig. 12. MIROC3.2 HIRES. (a) JFM total buoyancy flux, contoured each 1 mg/m^2/s upward from 5 mg/m^2/s. Regions with surface σ_θ = 25.7–26.7 for STMW are shown in colour. (b) JFM mixed layer depth (m) and February surface currents (m/s), with contours of surface σ_θ = 25.7–26.7. (c) JFM buoyancy flux due to heat (mg/m^2/s) out of the ocean, with contours of surface σ_θ = 25.7–26.7. (d) JFM buoyancy flux due to water/salt (mg/m^2/s) out of the ocean, with contours of surface σ_θ = 25.7–26.7. White contour is 0 of the flux.

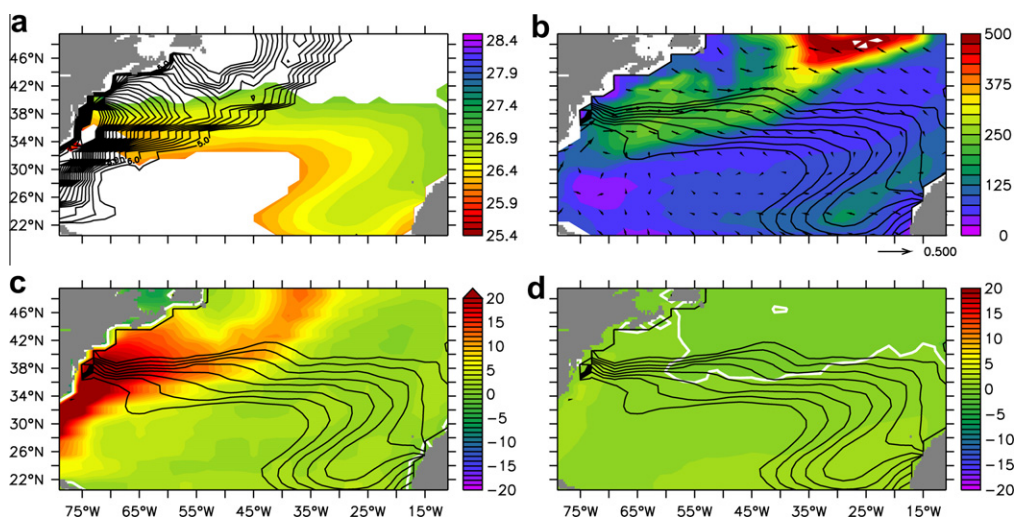

Fig. 13. CNRM CM3. (a) JFM total buoyancy flux, contoured each 1 mg/m^2/s upward from 5 mg/m^2/s. Regions with surface σ_θ = 26.2–26.9 for STMW are shown in colour. (b) JFM mixed layer depth (m) and February surface currents (m/s), with contours of σ_θ = 26.2–26.9. (c) JFM buoyancy flux due to heat (mg/m^2/s) out of the ocean, with contours of σ_θ = 26.2–26.9. (d) JFM buoyancy flux due to water/salt (mg/m^2/s) out of the ocean, with contours of σ_θ = 26.2–26.9. White contour is 0 of the flux.

is also well aligned with the region of deepest mixed layer depth in the northwest Sargasso Sea as well as the highest heat fluxes out of the ocean. Additionally the water flux shows evaporation out of the ocean in the western portion of the formation region. Notably, the extratropical precipitation band (as deduced from water flux) lies to the north of the STMW formation region. The range of densities found in the dense water pool off the North American coast fall between σ_θ = 26.0 and 26.5 kg/m^3, all of which density classes are in the region of WMTR negative slope. The high-density pool encompasses the location of that from observations; however, in the model it is more spatially extensive (Fig. 6).

CNRM CM3 (Fig. 13) only formed 6 Sv of STMW over its revised outcrop window. It did not form a pool of dense water offshore of the North American coast but rather displayed σ_θ nearly monotonically increasing with latitude. The appropriately-located region of heat flux and water flux produced a net formation of water in density classes σ_θ = 26.2–26.9 kg/m^3, but the quantity was not large. Fig. 13 shows the region of deepened mixed layer lay slightly to the east of the maximum fluxes. The region where outcropping σ_θ aligned with positive buoyancy flux lies inshore of that obtained from observations (Fig. 6).

4.3. STMW heat content and turnover times

In an effort to quantify the overall effect of these model biases in STMW formation (whatever their cause), various bulk quantities were calculated using volume-weighted integrations. For each model, within the geographic region of STMW, grid boxes containing mode water were identified using the following two criteria: (1) the temperature and salinity ranges appropriate to the σ_θ class for that model (Fig. 7); (2) vertical temperature gradient less than 0.006 °C/m. This second criterion was added to restrict the selected volumes to a thermostad and to permit comparisons with data in Kwon and Riser (2004). The portion of a profile within this region that met these conditions was identified as STMW; the thickness,

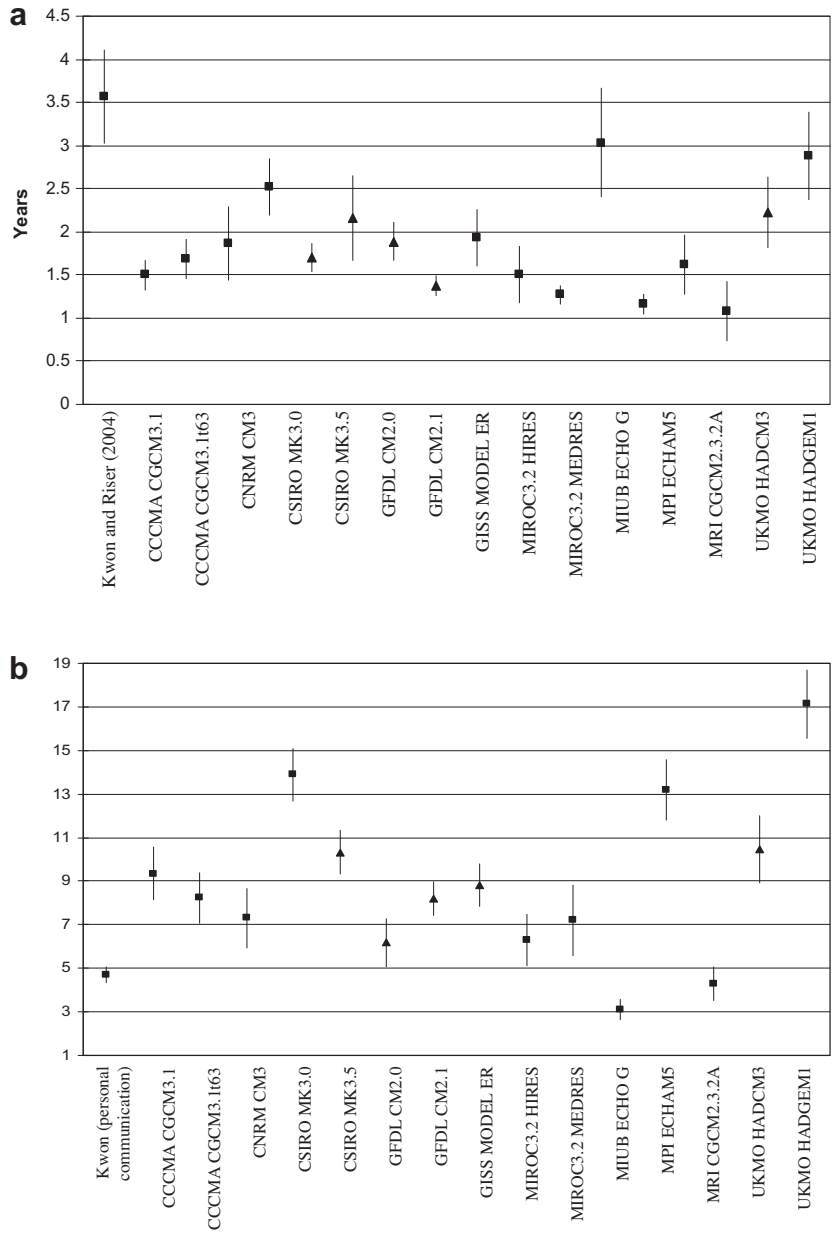

Fig. 14. (a) STMW turnover time for various models compared with Kwon and Riser (2004); time is calculated by annual maximum volume divided by annual production. Values are means; error bars give ranges of one standard deviation. Square data symbols indicate those models with a distinct (if small) secondary WMTR peak corresponding to STMW formation. Triangular data symbols indicate those models with broad, diffuse, or indiscernible STMW formation peak. (b) STMW maximum heat for various models compared with data from the same calculation as (a). Values are means; error bars give ranges of one standard deviation. Square data symbols indicate those models with a distinct (if small) secondary WMTR peak corresponding to STMW formation. Triangular data symbols indicate those models with broad, diffuse, or indiscernible STMW formation peak.

volume-weighted mean temperature, and heat content of that profile portion were calculated.

These individual profile calculations were summed to provide the monthly total volume, mean temperature, and total heat content could be calculated for each model, yielding means and standard deviation from the 20-year model results in consideration. Annual STMW production was calculated using the late winter maximum volume and subtracting the previous autumn minimum volume; STMW turnover time was calculated by dividing the late winter STMW maximum volume in each year by the STMW volume production each year.

$$T_{\text{turnover}} = \frac{V_{\max}}{V_{\text{produced}}} = \frac{V_{\max}}{V_{\max} - V_{\min}}$$

Twenty years of such calculations and models with multiple ensemble members provided means and standard deviations. Note for these turnover time calculations, if the autumn minimum volume $V_{\min}$ approaches 0 m^3, turnover time T_{turnover} approaches 1 year; if the autumn minimum volume $V_{\min}$ approaches $V_{\max}$, turnover time T_{turnover} gets large. The observed turnover time of 3.57 years (Kwon and Riser, 2004) implies an autumn minimum volume $V_{\min} = .72V_{\max}$, approximately ¾ the following winter maximum volume.

Fig. 14a shows STMW turnover time calculated for these models, compared with data. All the models have a shorter turnover time than calculated in Kwon and Riser (2004); most notably, model turnover times varied widely. Many models with shorter turnover times also displayed small formation rates for the lighter water type in Fig. 2 (e.g. CCCMA CGCM3.1, GISS MODEL ER, MIUB

ECHO G). In contrast, MRI CGCM2.3.2A had a pronounced water mass formation rate, but horizontal temperature transects (not shown) revealed that the model had difficulties maintaining a thermostad for STMW so the water mass did not meet this algorithm's gradient criterion.

Maximum (winter) heat contents for each model in Fig. 14b show generally higher heat content than the data. The models' heat contents were primarily driven by volume of STMW so these high quantities may reflect model discretization. The combination of high maximum heat content with short turnover times are due to the models' annual cycle of volume formation rates and high volume destruction rates (near complete destruction of the previous winter's STMW, hence little interannual retention of water properties). A water mass change each year is consistent with turnover times being on the close order of a year. These results suggest that climate models with extremely short turnover times would have little year-to-year memory of anomalous conditions, but would simply form STMW with properties dominated by the most recent year's conditions; their STMW heat content would have no memory of earlier years' NAO states. These models would hence miss the lagged correlation between NAO state and STMW properties found in Kwon and Riser (2004); air–sea feedbacks would be based only on most recent heat storage events.

5. Conclusions

This study of the mode water formation rates and processes for the suite of global coupled climate models in the CMIP3 multimodel dataset has shown considerable variability in the models' abilities to form mode waters at the appropriate densities or in the appropriate amounts. Using the WMTR calculations of Speer and Tziperman (1992) and Walin (1982), quantities of water created at various density classes were calculated for each model. The models formed SPMW and STMW at density classes that differed from those observed, and formed quantities of these water masses that varied widely. To understand the causes of these differences, we compared T–S properties of the water masses, air–sea fluxes and circulation patterns. The implications of the biases were explored in terms of the MOC in the case of SPMW, and heat content and overturn time in that of STMW. We acknowledge that there may be errors in the assessed mode water formation rates due to edge or diffusive fluxes; model-to-model differences in various models' treatments of the entrainment and lateral mixing processes and from model to data, could cause the wide range of water properties and formation rates for both STMW and SPMW. However, without archived diffusivities or model-specific logical grids on which to compute the importance of these flux terms, we were unable to study their relative contributions to the density budget.

For SPMW, density errors are primarily due to salinity errors as the phase change (freezing) prevents the models from cooling water past a minimum temperature. More importantly, models varied in location of SPMW formation: some models formed SPMW west of Great Britain rather than in the Labrador Sea. These positional differences of the model outcropping regions resulted from anomalous model currents and inappropriate preconditioning of the water west of Great Britain. These positional differences of water mass formation suggested general circulation problems, notably varying the degree of Nordic Sea involvement in the MOC.

The models displayed a wider range of variation in STMW formation as that process relies on the precise coupling between ocean and atmosphere heat and water fluxes. If atmospheric fluxes are mis-aligned with the ocean's western boundary current separation, the processes that form the STMW pool will be spatially out of phase and less effective at producing that water mass. Various biases can occur, any one of which negatively affects STMW production. Mispositioning of the Gulf Stream separation from the North American coast or mis-alignment of heat fluxes out of the ocean due to cold air outbreaks can decrease the model's ability to form STMW. Extensive diagnostic and/or model sensitivity studies would be required for each model to determine the causes of heat or water flux biases, or Gulf Stream separation problems; however, such studies are not possible as we are limited to the output fields in the CMIP archive.

Rather than pursuing an in depth assessment of the causes of STMW formation problems, we examined their implications by looking at STMW heat content and turnover time. The mode waters with their vertical extent represent large repositories of heat which can then be available either for advection due to the Gulf Stream and remote re-emergence (De Coetlogon and Frankignoul, 2003) or transfer to the atmosphere. The short, in many cases extremely short, STMW turnover times cast doubt on the models' abilities to correctly reproduce interannual modes of variability, in particular the correct NAO feedbacks, and to correctly model the observed re-emergence of a previous year's temperature anomaly following the summer surface heating.

Many of the problems with currents and vertical mixing noted in these models are characteristic of ocean models having horizontal grid spacing on the order of one degree. Higher-resolution models capable of largely resolving mesoscale ocean eddies, together with more advanced mixing parameterizations, are required to better duplicate these ocean physical processes that are so important to the global ocean circulation as well as heat transfers to the atmosphere. An assessment of the abilities of such models to reproduce SPMW and STMW formation processes would provide considerable insight into their ability to correctly predict changes

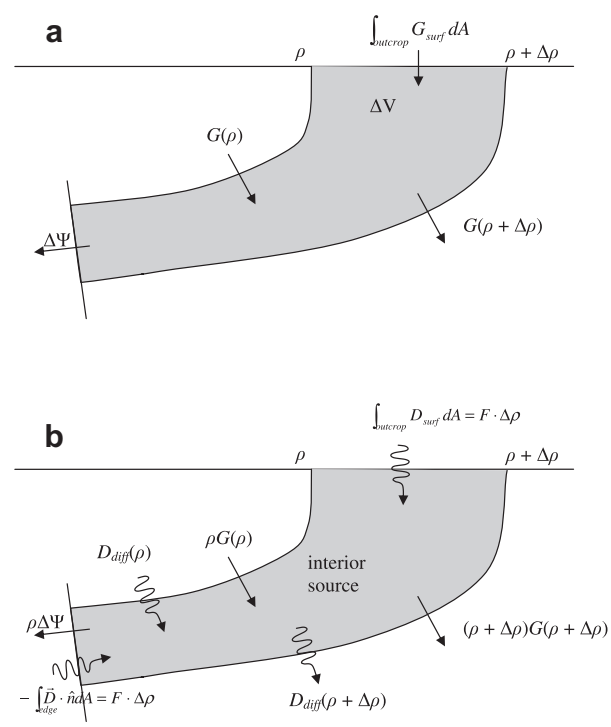

Fig. 15. Schematics of water mass transformation, redrawn based on the depictions of Large and Nurser (2001, their Fig. 5.1.1). (a) Volume budget. Layer volume depends on divergence of diapycnal volume flux G across density surfaces, volume flux $\Delta\Psi$ exiting the domain, and the surface fresh water influx G_{surf} integrated over the outcrop. (b) Mass budget. Layer mass depends on advection from the diapycnal volume flux ρG and the mass exiting the domain $\rho\Delta\Psi$, the divergence of the diffusive mass fluxes D, the surface density influx D_{surf} integrated over the outcrop, the density flux through the edges of the control volume into the layer $F\Delta\rho$, and the interior density source.

in these heat storage/advection processes as heat and water fluxes as well as wind stresses, change with time, and hence to correctly predict changes in global ocean circulation as the climate state changes.

Acknowledgements

We acknowledge the modelling groups, the Program for Climate Model Diagnosis and Intercomparison (PCMDI) and the WCRP's Working Group on Coupled Modelling (WGCM) for their roles in making available the WCRP CMIP3 multi-model dataset. Support of this dataset is provided by the Office of Science, US Department of Energy. NODC_WOA94 data were provided by the NOAA/OAR/ESRL PSD, Boulder, Colorado, USA, from their Web site at http://www.cdc.noaa.gov/. J.C.C.'s funding was provided by the Lawrence Livermore Military Academic Research Associate program and the DOE Office of Biological and Environmental Research. J.L.M. was supported by the DOE Office of Biological and Environmental Research through a sub-contract from LLNL/PCMDI to SIO. The authors greatly appreciate the helpful comments of Lynne Talley (SIO), Peter Gleckler (LLNL), Ivana Cerovecki (SIO), and Detelina Ivanova (LLNL) as well as the reviewers and the Editor for their comments and suggestions, which greatly improved the quality of this work. Young-Oh Kwon (WHOI) provided measures of the STMW overturn and heat content from data sources. Frank Bryan (NCAR) provided the water mass transformation code. The authors additionally thank Peter Braccio for his help with the generation of the final figures.

Appendix

The Walin (1982) framework is used in this paper to calculate water mass transformation and formation rates. The former is the rate at which water is transformed from one density class to another via air–sea heat and freshwater fluxes. The divergence of the transformation rate yields the rate at which a given density class is created or destroyed via these fluxes (the formation rate). We largely follow the derivations and notation of Nurser et al. (1999) and Large and Nurser (2001); only the salient details of their derivations are provided here.

Consider two potential density surfaces, ρ and $\rho + \Delta\rho$, that outcrop at the sea surface in a region with a deeper open boundary (see Fig. 15(a) that we have redrawn, based on depictions in Fig. 5.1.1 of Large and Nurser (2001)). First we make the Boussinesq approximation and assume compressibility and then we formulate a volume budget for the control volume bounded by isopycnals ρ and $\rho + \Delta\rho$, the ocean surface, and the open boundary. It is:

$$\left(\frac{\partial \Delta V}{\partial t} + \Delta\Psi\right) = G(\rho) - G(\rho + \Delta\rho) + \int_{\text{outcrop}} G_{\text{surf}} dA \tag{1}$$

where ΔV is the volume of fluid between ρ and $\rho + \Delta\rho$, $\Delta\Psi$ is the volume flux of fluid leaving the volume, $G(\rho)$ and $G(\rho + \Delta\rho)$ are the diapycnal volume fluxes across the ρ and $\rho + \Delta\rho$ isopycnals, and $\int_{\text{outcrop}} G_{\text{surf}} dA$ is the net surface influx of volume at the surface over the outcrop with ρ_0 mean density and F_{in} the net freshwater input ($G_{\text{surf}} = \rho_0^{-1} F_{in}$). The water mass formation, M, can be obtained by adding the volume inflation and outflow terms (first and second terms on the right hand side of Eq. (2)):

$$M\Delta\rho = \frac{\partial V}{\partial t} + \Delta\Psi. \tag{2}$$

We combine Eqs. (1) and (2) to obtain the water mass formation rate per unit density, $M(\rho)$, that consists of the convergence of the diapycnal volume flux and the surface volume flux per unit density:

$$M(\rho) = -\frac{\partial G}{\partial \rho} + \lim_{\Delta\rho \to 0} \frac{1}{\Delta\rho} \int_{\text{outcrop}} G_{\text{surf}} dA. \tag{3}$$

The first term on the right hand side generally dominates the second so the second is usually neglected, leaving

$$M(\rho) = -\partial G / \partial \rho. \tag{4}$$

Next we examine the density budget for this same control volume (Fig. 1b) where advective and diffusive fluxes balance:

$$\begin{aligned}\underbrace{\left(\frac{\partial \Delta V}{\partial t} + \Delta\Psi\right)\rho}_{\text{density content gain of layer}} &= \underbrace{\rho G(\rho) - (\rho + \Delta\rho) G(\rho + \Delta\rho)}_{\text{outward advective density fluxes}} \\ &+ \underbrace{D_{diff}(\rho) - D_{diff}(\rho + \Delta\rho) + \int \vec{D}_{\text{edge}} \cdot \hat{n} dA + \int_{\text{outcrop}} D_{\text{surf}} dA}_{\text{diffusive influx of density}} \\ &+ \underbrace{\Delta\rho \cdot \rho \lim_{\Delta\rho \to 0} \frac{1}{\Delta\rho} \int_{\text{outcrop}} G_{\text{surf}} dA}_{\text{surface advective influx of density}} + \text{interior sources of density}\end{aligned} \tag{5}$$

where $D_{\text{diff}}(\rho)$ and $D_{\text{diff}}(\rho + \Delta\rho)$ are the area-integrated diapycnal diffusive density fluxes across the two potential density surfaces, and $\int_{\text{outcrop}} D_{\text{surf}} dA$ is the total surface density influx between the bounding isopycnals. We also include the diffusive influxes at the edge of the control volume, advective density fluxes at the surface, and interior density sources (cabbeling).

This equation can be rewritten as

$$M\rho + \frac{\partial}{\partial \rho}(\rho G) = -\frac{\partial D_{\text{diff}}}{\partial \rho} + F(\rho) + F_{\text{edge}} + C \tag{6}$$

where

$$F(\rho) = \lim_{\Delta\rho \to 0} \frac{1}{\Delta\rho} \int_{\text{outcrop}} D_{\text{surf}} dA$$

represents the surface density influx per unit of density and is the water mass transformation rate driven by air–sea fluxes. $F_{\text{edge}}(\rho)$ represents the diffusive influx per unit of ρ through the control-volume edge into the layer and $C(\rho)$ is the cabbeling source term.

Using Eq. (4) we obtain:

$$G(\rho) = -\frac{\partial D_{\text{diff}}}{\partial \rho} + F(\rho) + F_{\text{edge}} + C. \tag{7}$$

The importance of each of the terms on the right hand side of Eq. (7) varies according to the dominant physical processes in a particular setting. Typically the cabbeling source term is small and is usually neglected (Nurser et al., 1999). The importance of the $F_{\text{edge}}(\rho)$ term depends on the slope of the isopycnals forming the control volume in the thermocline: the steeper their slopes, the weaker the horizontal diffusive flux (Large and Nurser, 2001) resulting in relatively small edge fluxes. This leaves us with:

$$G(\rho) = -\frac{\partial D_{\text{diff}}}{\partial \rho} + F(\rho). \tag{8}$$

In the steady state limit, $G(\rho) = 0$ and we have a balance between F and the convergence of the diffusive fluxes across the bounding isopycnals of the control volume (Marshall et al., 1999).

Various studies have been undertaken to understand the relative importance of the mixing term. Garrett et al. (1995) performed a scale analysis and showed that it is small if the slope of the mixed layer base is small compared to the slope of the isopycnals in the mixed layer. Speer (1997) used climatology data to suggest that mixing is indistinguishable from zero in the range of thermocline densities. Garret and Tandon (1997) performed analyses of buoyancy profiles suggesting that subduction from the base of the mixed layer is not large. Importantly for our study, Nurser et al.

(1999) calculated surface fluxes for the North Atlantic and found that they were considerably larger (order of magnitude) than estimates of lateral mixing and seasonal entrainment. They further used a coupled mixed layer and isopycnic model of the North Atlantic to diagnose thermocline diapycnal density flux, entrainment density flux, and lateral density flux; for the Sargasso Sea, water mass formation rate due to mixing processes made relatively minor contributions compared to the formation rate due to surface forcing. Similarly, over the Labrador and Irminger Seas, they found that mixing again played a relatively minor role. So finally when diapycnal density fluxes, edge fluxes, and cabbeling are small relative to F, then the formation rate per unit density, $M(\rho)$, can be written in terms of the surface fluxes as

$$M(\rho) = -\frac{\partial F}{\partial \rho}. \tag{9}$$

References

Alexander, M.A., Deser, C., 1995. A mechanism for the recurrence of wintertime midlatitude SST anomalies. J. Phys. Oceanogr. 25, 122–137.

Berry, D.I., Kent, E.C., 2009. A new air–sea interaction gridded dataset from ICOADS with uncertainty estimates. Bull. Am. Meteorol. Soc. 90, 645–656.

Blanke, B., Delecluse, P., 1993. Variability of the tropical Atlantic Ocean simulated by a general circulation model with two different mixed-layer physics. J. Phys. Oceanogr. 23, 1363–1388.

Brambilla, E., Talley, L.D., 2008. Subpolar mode water in the northeastern Atlantic 1. Averaged properties and mean circulation.. J. Geophys. Res. 113, C04025. doi:10.1029/2006JC004062.

Brambilla, E., Talley, L.D., Robbins, P.E., 2008. Subpolar mode water in the northeastern Atlantic: 2. Origin and transformation. J. Geophys. Res. 113, C04026. doi:10.1029/2006JC004063.

Bryan, F.O., Danabasoglu, G., Nakashiki, N., Yoshida, Y., Kim, D.-H., Tsutsui, J., Doney, S.C., 2006. Response of the North Atlantic thermohaline circulation and ventilation to increasing carbon dioxide in CCSM3. J. Climate 19, 2382–2397.

Bryan, K., Lewis, L.J., 1979. A water mass model of the world ocean. J. Geophys. Res. 84, 2503–2517.

Cerovecki, I., Talley, L.D., Mazloff, M.R., Maze, G., 2011. Subantarctic Mode Water formation in a Data Assimilating Model.

Cox, M.D., 1987. Isopycnal diffusion in a *z*-coordinate model. Ocean Modell. 74, 1–5 (unpublished manuscript).

De Boyer Montégut, C., Madec, G., Fischer, A.S., Lazar, A., Iudicone, D., 2004. Mixed layer depth over the global ocean: an examination of profile data and a profile-based climatology. J. Geophys. Res. 109, C12003. doi:10.1029/2004JC002378.

De Coetlogon, G., Frankignoul, C., 2003. The persistence of winter sea surface temperature in the North Atlantic. J. Climate 16, 1364–1377.

Doney, S.C., Large, W.G., Bryan, F.O., 1998. Surface ocean fluxes and water-mass transformation rates in the coupled NCAR climate system model. J. Climate 11, 1420–1441.

Forget, G., Maze, G., Buckley, M., Marshall, J., 2011. Estimated seasonal cycle of North Atlantic eighteen degree water volume. J. Phys. Oceanogr. 41, 269–286.

Garrett, C., Speer, K., Tragou, E., 1995. The relationship between water mass formation and the surface buoyancy flux, with application to the Phillips' Red Sea model. J. Phys. Oceanogr. 25, 1696–1705.

Garret, C., Tandon, A., 1997. The effects on water mass formation of surface mixed layer time-dependence and entrainment fluxes. Deep-Sea Res. I 44, 1991–2006.

Gent, P.R., McWilliams, J.C., 1990. Isopycnal mixing in ocean circulation models. J. Phys. Oceanogr. 20, 150–155.

Gent, P.R., Willebrand, J., McDougall, T.J., McWilliams, J.C., 1995. Parameterizing eddy-induced tracer transports in ocean circulation models. J. Phys. Oceanogr. 25, 463–474.

Griffies, S.M., 1998. The Gent-McWilliams skew flux. J. Phys. Oceanogr. 28, 831–841.

Griffies, S.M., Gnanadesikan, A., Pacanowski, R.C., Larichev, V.D., Dukowicz, J.K., Smith, R.D., 1998. Isoneutral diffusion in a *z*-coordinate ocean model. J. Phys. Oceanogr. 28, 805–830.

Hanawa, K., Talley, L.D., 2001. Mode waters. In: Siedler, J.C.G., Gould, J. (Eds.), Ocean Circulation and Climate – Observing and Modeling the Global Ocean. Academic Press, San Diego, pp. 372–386.

Haines, K., Old, C., 2005. Diagnosing natural variability of North Atlantic water masses in HadCM3. J. Climate 18, 1925–1941.

Joyce, T.M., Deser, C., Spall, M.A., 2000. The relation between decadal variability of subtropical mode water and the North Atlantic oscillation. J. Climate 13, 2550–2569.

Kraus, E.B., Turner, J.S., 1967. A one-dimensional model of the seasonal thermocline II. The general theory and its consequences. Tellus 19, 98–106.

Kwon, Y.-O., Riser, S., 2004. North Atlantic Subtropical Mode Water: a history of ocean–atmosphere interaction 1961–2000. Geophys. Res. Lett. 31, L19307. doi:10.1029/2004GL02116.

Large, W.G., McWilliams, J.C., Doney, S.C., 1994. Oceanic vertical mixing: a review and a model with a nonlocal boundary layer parameterization. Rev. Geophys. 32, 363–403.

Large, W.G., Nurser, A.J.G., 2001. Ocean surface water mass transformation. In: Siedler, J.C.G., Gould, J. (Eds.), Ocean Circulation and Climate – Observing and Modeling the Global Ocean. Academic Press, San Diego, pp. 317–336.

Levitus, S., 1982. Climatological Atlas of the World Ocean. NOAA Prof. Paper 13, National Oceanic and Atmospheric Administration, Rockville, MD, 173+XV pp.

Lumpkin, R., Speer, K., 2003. Large-scale vertical and horizontal circulation in the North Atlantic Ocean. J. Phys. Oceanogr. 33, 1902–1920.

Lumpkin, R., Speer, K., 2007. Global ocean meridional overturning. J. Phys. Oceanogr. 37, 2550–2562.

Marsh, R., Josey, S.A., Nurser, A.J.G., de Cuevas, B.A., Coward, A.C., 2005. Water mass transformation in the North Atlantic over 1985–2002 simulated in an eddy-permitting model. Ocean Sci. 1, 127–144.

Marshall, J., Jamous, D., Nilsson, J., 1999. Reconciling thermodynamic and dynamic methods of computation of water-mass transformation rates. Deep-Sea Res. I 46, 545–572.

Maze, G., Forget, G., Buckley, M., Marshall, J., 2009. Using transformation and formation maps to study the role of air–sea heat fluxes in North Atlantic Eighteen Degree Water formation. J. Phys. Oceanogr. 39, 1818–1835.

McCartney, M.S., 1982. The subtropical recirculation of mode waters. J. Mar. Res. 40 (Suppl.), 427–464.

McCartney, M.S., Mauritzen, C., 2001. On the origin of the warm inflow to the Nordic Seas. Prog. Oceanogr. 51, 125–214.

McCartney, M.S., Talley, L.D., 1982. The subpolar mode water of the North Atlantic Ocean. J. Phys. Oceanogr 12, 1169–1188.

McCartney, M.S., Talley, L.D., 1984. Warm-to-cold water conversion in the North Atlantic Ocean. J. Phys. Oceanogr 14, 922–935.

Meehl, G.A., Covey, C., Delworth, T., Latif, M., McAvaney, B., Mitchell, J.F.B., Stouffer, R.J., Taylor, K.E., 2007. The WCRP CMIP3 multi-model dataset: a new era in climate change research. Bull. Am. Meterol. Soc. 88, 1383–1394.

Mellor, G.L., Durbin, P.A., 1975. The structure and dynamics of the ocean surface mixed layer. J. Phys. Oceanogr. 5, 718–728.

Mellor, G.L., Yamada, T., 1974. A hierarchy of turbulence closure models for planetary boundary layers. J. Atmos. Sci. 31, 1791–1806.

Monterey, G.I., Levitus, S., 1997. Climatological Cycle of Mixed Layer Depth in the World Ocean. US Gov. Printing Office, NOAA NESDIS, 5pp.

Noh, Y., Kim, H.J., 1999. Simulations of temperature and turbulence structure of the oceanic boundary layer with the improved near-surface process. J. Geophys. Res. 104 (15), 15,621–15,634.

Nurser, A.J.G., Marsh, R., Williams, R.G., 1999. Diagnosing water mass formation from air–sea fluxes and surface mixing. J. Phys. Oceanogr. 29, 1468–1487.

Oberhuber, J.M., 1988. An Atlas Based on the COADS Data Set: The Budgets of Buoyancy and Turbulent Kinetic Energy at the Surface of the Global Ocean. Max Planck Institute for Meteorology Report, 15, Hamburg, 200 pp.

Pacanowski, R.C., Philander, S.G.H., 1981. Parameterization of vertical mixing in numerical models of tropical oceans. J. Phys. Oceanogr. 11, 1443–1451.

Peng, G., Chassignet, E.P., Kwon, Y.-O., Riser, S.C., 2006. Investigation of variability of the North Atlantic subtropical mode water using profiling float data and numerical model output. Ocean Modell. 13, 65–85.

Read, J.F., 2001. CONVEX-91: water masses and circulation of the Northeast Atlantic subpolar gyre. Prog. Oceanogr. 48, 461–510.

Roberts, M.J., Banks, H., Gedney, N., Gregory, J., Hill, R., Mullerworth, S., Pardaens, A., Rickard, G., Thorpe, R., Wood, R., 2004. Impact of an eddy-permitting ocean resolution on control and climate change simulations with a global coupled GCM. J. Climate 17, 3–20.

Schmitz, W.J., McCartney, M.S., 1993. On the North Atlantic circulation. Rev. Geophys. 31, 29–49.

Speer, K.G., 1997. A note on average cross-isopycnal mixing in the North Atlantic Ocean. Deep-Sea Res. I 44, 1981–1990.

Speer, K.G., Isemer, H.J., Biastoch, A., 1995. Water mass formation from revised COADS data. J. Phys. Oceanogr. 25, 2444–2457.

Speer, K.G., Tziperman, E., 1992. Rates of water mass formation in the North Atlantic Ocean. J. Phys. Oceanogr. 22, 93–104.

Talley, L.D., 1996. North Atlantic circulation and variability, reviewed for the CNLS conference. Physica D 98, 625–646.

Talley, L.D., 1999. Mode waters in the subpolar North Atlantic in historical data and during the WOCE period. WOCE Newsletter 37, 3–6.

Talley, L.D., McCartney, M.S., 1982. Distribution and circulation of Labrador Sea Water. J. Phys. Oceanogr. 12, 1189–1205.

Talley, L.D., Raymer, M.E., 1982. Eighteen degree water variability. J. Mar. Res. 40 (Suppl.), 757–775.

Taylor, B.N. Kuyatt, C.E., 1994. Guidelines for Evaluating and Expressing the Uncertainty of NIST Results. NIST Technical Note 1297, US GPO, Washington, DC, 20 pp.

Thompson, C.W., 1877. The Voyage of the "Challenger," vol. 1. The Atlantic, Macmillan, Old Tappan, NJ, 424 pp.

Timlin, M.S., Alexander, M.A., Deser, C., 2002. On the reemergence of North Atlantic SST anomalies. J. Climate 15, 2707–2712.

Visbeck, M., Marshall, J., Haine, T., 1997. Specification of eddy transfer coefficients in coarse-resolution ocean circulation models. J. Phys. Oceanogr. 27, 381–402.

Walin, G., 1982. On the relation between sea-surface heat flow and thermal circulation in the ocean. Tellus 34, 187–195.

Wilson, S.G., 2000. How ocean vertical mixing and accumulation of warm surface water influence the "sharpness" of the equatorial thermocline. J. Climate 13, 3638–3656.
Wilson, S.G., 2002. Evaluation of various vertical mixing parameterizations in a tropical Pacific Ocean GCM. Ocean Modell. 4, 291–311.
Woodruff, S.D., Slutz, R.J., Jenne, R.L., Steurer, P.M., 1987. A comprehensive ocean-atmosphere data set. Bull. Am. Meteorol. Soc. 68, 521–527.
Wright, D.K., 1997. A new eddy mixing parameterization and ocean general circulation model. WOCE Newsletter 26, 27–29.
Wright, P., 1988. An Atlas Based on the COADS Data Set: Fields of Mean Wind, Cloudiness, and Humidity at the Surface of the Global Ocean. Max Planck Institute Report, 14, Hamburg, 70 pp.
Worthington, L.V., 1959. The 18° water in the Sargasso Sea. Deep Sea Res. 5, 297–305.
Worthington, L.V., 1977. The intensification of the Gulf Stream after the winter of 1976–1977. Nature 270, 415–417.